FORCE-INDUCED ACOUSTIC PHONON TRANSPORT ACROSS SINGLE-DIGIT NANOMETRE VACUUM GAPS

A PREPRINT

Amun Jarzembski[1,†] **Takuro Tokunaga**[1,†] **Jacob Crossley**[1] **Jeonghoon Yun**[2] **Cedric Shaskey**[1]

Ryan A. Murdick[3] **Inkyu Park**[2] **Mathieu Francoeur**[1,*] **Keunhan Park**[1,*]

November 18, 2021

[1]*Department of Mechanical Engineering, University of Utah, Salt Lake City, UT 84112, USA.*
[2]*Department of Mechanical Engineering, Korea Advanced Institute of Science and Technology, Daejeon 305-701, South Korea.*
[3]*Montana Instruments, Bozeman, MT 59715, USA*
[†]*These authors contributed equally to this work.*
[*]*To whom correspondance should be addressed: mfrancoeur@mech.utah.edu and kpark@mech.utah.edu.*

ABSTRACT

Heat transfer between bodies separated by nanoscale vacuum gap distances has been extensively studied for potential applications in thermal management [1, 2], energy conversion [3] and data storage [4]. For vacuum gap distances down to 20 nm, state-of-the-art experiments demonstrated that heat transport is mediated by near-field thermal radiation, which can exceed Planck's blackbody limit due to the tunneling of evanescent electromagnetic waves [5–13]. However, at sub-10-nm vacuum gap distances, current measurements are in disagreement on the mechanisms driving thermal transport [14–18]. While it has been hypothesized that acoustic phonon transport across single-digit nanometre vacuum gaps (or acoustic phonon tunneling) can dominate heat transfer [19–23], the underlying physics of this phenomenon and its experimental demonstration are still unexplored. Here, we use a custom-built high-vacuum shear force microscope (HV-SFM) to measure heat transfer between a silicon (Si) tip and a feedback-controlled platinum (Pt) nanoheater [24] in the near-contact, asperity-contact, and bulk-contact regimes. We demonstrate that in the near-contact regime (i.e., single-digit nanometre or smaller vacuum gaps before making asperity contact), heat transfer between Si and Pt surfaces is dominated by force-induced acoustic phonon transport that exceeds near-field thermal radiation predictions by up to three orders of magnitude. The measured thermal conductance shows a gap dependence of $d^{-5.7\pm1.1}$ in the near-contact regime, which is consistent with acoustic phonon transport modelling based on the atomistic Green's function (AGF) framework. Our work suggests the possibility of engineering heat transfer across single-digit nanometre vacuum gaps with external force stimuli, which can make transformative impacts to the development of emerging thermal management technologies.

Introduction

Over the past decades, radiative heat transfer in the near-field regime (i.e., vacuum gap sizes smaller than Wien's wavelength) has been fundamentally understood within the fluctuational electrodynamics (FE) framework [25] and experimentally confirmed for gap distances as small as 20 nm [5–13]. In contrast, phonons become the dominant heat carrier when two objects are brought into contact [26], suggesting that there should be a transition from near-field thermal radiation to phonon heat conduction in the near-contact regime. Fundamental understanding of this transition, however, has been severely limited by experimental challenges, which has led to disagreement between experimental data and their interpretation [14–18]. Kim *et al.* [14] measured heat transfer for silica, silicon nitride, and gold surfaces,

observing good agreement with FE down to a vacuum gap of $\sim$2 nm. This result is in contradiction to experiments conducted by Kloppstech *et al.* [17], who reported heat transfer between gold surfaces exceeding FE by more than four orders of magnitude for vacuum gaps from 7 nm down to 0.2 nm. However, the lack of comprehensive modeling has triggered debates regarding the thermal transport mechanism responsible for such large heat transfer [18]. Although recent studies have suggested acoustic phonon transport across single-digit nanometre vacuum gaps as a plausible radiation-to-conduction transition mechanism [19–23], only one indirect thermal transport measurement attempted to identify the so-called phonon tunneling phenomena [15]. Here, we present comprehensive experimental and theoretical results unambiguously demonstrating that force-induced acoustic phonon transport can dominate heat transfer in the near-contact regime. To this end, we uniquely implement feedback-controlled Pt nanoheaters in a HV-SFM platform for heat transfer measurements (Fig. 1a), and quantitatively compare the obtained experimental data with theory based on the AGF and FE frameworks.

Experimental Setup

The HV-SFM adopts a vertically aligned quartz tuning fork (QTF) resonator probe with a low-doped Si tip rigidly mounted to its free end for sensitive tip-sample lateral force measurement [27]. The QTF probes have a quality factor of $\sim$4000 in a high-vacuum condition (5×10^{-6} Torr), which allows tip-sample gap control with single-angstrom resolution by monitoring their resonance frequency shift, Δf (see Methods). The Si tip is modified to a flat-top, 210 ± 30 nm in width, to secure a sufficient heat transfer area (Fig. 1b). The Pt nanoheater has a sensing region of $\sim$300 nm $\times$ 500 nm between the two inner electrodes (yellow dashed box in Figs. 1c and d) enabling a four-probe electrical resistance measurement (see Supplementary Section 1). The nanoheater's sensing region temperature ($T_{\rm NT}$) is maintained constant by feedback-controlling the Joule-heating electrical power to compensate tip-induced thermal transport [24]. The nominal thermal resistance of the nanoheater sensing region is $\sim$0.5 K/μW, which is equivalent to a $\pm 1\sigma$ DC power resolution of $\sim$60 nW (see Supplementary Section 2). The benefit of combining the feedback-controlled nanoheater and HV-SFM platform is the simultaneous measurement of tip-induced thermal transport and conservative tip-nanoheater lateral force interactions. The high rigidity of the QTF probe enables stable control of sub-nanometre gap distances, which is not possible in cantilever-based method due to snap-in contact [14]. In addition, HV-SFM is not limited to electrically conductive materials as required by the electron tunneling methodologies [15–18].

Results and Discussion

In order to consistently describe the thermal and force interactions around contact, we define the tip-nanoheater gap (d) as the distance between the flattened Si tip and the mean line of the nanoheater surface profile (Fig. 2a). The nominal surface profile of the nanoheaters used for this study has a peak roughness of 5.0$\pm$0.1 nm within a 98.5% confidence interval (see Methods). The bulk-contact (BC) regime is then defined as $d \leq 0$, where the majority of Pt surface asperities are in solid contact with the Si surface (Fig. 2b). The near-contact (NC) regime is where d is larger than the surface roughness (i.e., $d \gtrsim 5$ nm) to ensure no contact between surface asperities. The asperity-contact (AC) regime resides between the BC and NC regimes (i.e., $0 < d \lesssim 5$ nm). Fig. 2c shows the $T_{\rm NT}$ trace as the nanoheater is approached to the Si tip ($T_{\rm tip} \approx 295$ K: see Supplementary Section 4). The approaching speed of the sample stage is 0.75 nm/s to provide sufficient time to stabilize $T_{\rm NT}$ at 467.13 K within $\pm$50 mK accuracy. The $T_{\rm NT}$ signal drops at a point where the feedback controller cannot follow the abrupt increase of heat transfer through the bulk-contacted Si-Pt interfaces. The onset of the BC point can be also determined by observing the Δf signal of the QTF (Fig. 2d). While the Δf monotonically increases as the nanoheater approaches the tip, its z-derivative in the inset clearly shows the drastic drops at the thermally determined BC point. The concurrent thermal and mechanical signal changes indicate that BC can be unambiguously determined as a reference point for the tip-nanoheater gap (i.e., $d = 0$).

The heat transfer rate from the nanoheater sensing region to the tip ($Q_{\rm tip}$) is measured by monitoring the change of the power dissipation in the nanoheater (see Supplementary Section 3) [24]. In Fig. 2e, the experimental thermal conductance, defined as $G_{\rm exp} = Q_{\rm tip}/\Delta T$, exhibits a monotonic increasing trend with decreasing d and approaches the adjusted BC thermal conductance ($G^*_{\rm BC}$) of 74.1 $\pm$ 5.1 nW/K. It should be noted that $G^*_{\rm BC}$ was separately measured using a cantilever probe and is adjusted to consider the difference in tip geometry (see Methods). On a log-log scale, $G_{\rm exp}$ follows a $d^{-5.7}$ power law for 5 nm $\lesssim d \lesssim$ 7 nm in the NC regime (Fig. 2f). At $d \approx 5$ nm, the $d^{-5.7}$ trend saturates, indicating the onset of the AC regime. In order to verify the reproducibility of the observed NC gap dependence (d^n), we repeated the measurement 80 times using three different tip-nanoheater sets and extracted n values. Each data fits well with the d^n function in the NC regime as quantified by an average R^2-value of 0.87. Fig. 2g shows the histogram of the n values, which is well represented by a Gaussian distribution to yield $n = -5.7 \pm 1.1$.

The obtained $G_{\rm exp}$ and its gap dependence cannot be explained via FE-based models for tip-plane near-field radiative heat transfer [5, 14, 28, 29]. To elucidate the physics underlying our experimental results, we compute the heat transfer

coefficient of force-induced acoustic phonon transport by applying the AGF method [30] for the one-dimensional (1D) Si-Pt atomic chain system (Fig. 3a). The Lennard-Jones (L-J), Casimir, and Coulomb forces are considered to virtually connect the Pt and Si atomic chains, which allows acoustic phonon transport across the interatomic vacuum distance, δ (see Methods and Supplementary Sections 5 & 6) [21]. While the L-J and Casimir forces drive heat transfer for $\delta < 1.2$ nm, the Coulomb force becomes a dominant contributor for larger δ (i.e., 1.2 nm $< \delta <$ 10 nm). This significant contribution of the Coulomb force arises from surface charges induced by the local voltage bias (0.8 V) at the nanoheater sensing region under Joule heating. Here, we assume that the Coulomb force vanishes for $\delta < 1.2$ nm due to surface charge neutralization between the nanoheater and tip (see Supplementary Section 5). As a result, force-induced acoustic phonon heat transfer between Pt and Si surfaces can exceed near-field thermal radiation calculated with FE for interatomic distances up to $\delta \sim 10$ nm. The calculated heat transfer coefficients follow power laws ranging from $\delta^{-3.8}$ to $\delta^{-7.6}$, illustrating that the experimental value of $d^{-5.7}$ could be indicative of force-induced acoustic phonon transport. Fig. 3b shows the phonon transmission function calculated by the AGF method, where the dominant frequency range of phonon transmission is below $\sim$10 cm^{-1} at $\delta = 0.5$ nm. The phonon dispersion curves and density of states (DoS) for bulk Pt and Si (Figs. 3c,d), calculated via the density functional theory (DFT), confirm that acoustic phonons are the dominant heat carriers across the vacuum distance in the NC regime. Note that the heat transfer coefficient due to electron tunneling was found to be negligible compared to near-field radiation and acoustic phonon transport (see Supplementary Section 7).

The theoretical thermal conductance, G_{theory}, is determined using the Derjaguin approximation based on the measured nanoheater surface roughness distribution (see Methods). Fig. 4a shows excellent agreement between G_{exp} and G_{theory} on a linear-linear and log-log scale (inset). In the NC regime, G_{theory} reproduces the gap-dependence of $d^{-5.7}$ observed in G_{exp}, confirming our measurement of force-induced acoustic phonon transport between Pt and Si surfaces. The saturation of G_{exp} in the AC regime can also be theoretically explained by calculating phonon conduction through asperity-contacted Si-Pt interfaces (G_{AC}). Fig. 4b shows the AC thermal conductance ratio ($G_{\mathrm{AC}}/G_{\mathrm{theory}}$) and asperity contact ratio ($A_{\mathrm{AC}}/A_{\mathrm{tip}}$, where A_{AC} is the asperity-contact area and A_{tip} is the total tip area) as a function of d. While both $G_{\mathrm{AC}}/G_{\mathrm{theory}}$ and $A_{\mathrm{AC}}/A_{\mathrm{tip}}$ in the NC regime are 0% signifying non-contact heat transfer, they start to increase as the gap distance is further reduced in the AC regime. At $d = 0$, A_{AC} reaches $\sim$60% of A_{tip} while G_{AC} contributes to $\sim$90% of G_{theory}, which provides theoretical evidence of the experimentally determined BC point.

Fig. 4c separates the contributions of each force to G_{theory} in addition to FE. The main contributors in the AC regime are the short range L-J and Casimir forces between Si and Pt atoms. However, the Coulomb force becomes a dominant contributor in the NC regime, allowing force-induced acoustic phonon transport to exceed near-field thermal radiation by up to three orders of magnitude. When considering the origin of the Coulomb force, this finding strongly suggests the possibility of enhancing heat flow in the NC regime with external force stimuli, such as electrostatic and magnetic forces. Fig. 4d further demonstrates the strong correlation between tip-surface heat transfer and force interactions by comparing G_{exp} to the simultaneously acquired Δf of the QTF. In the AC regime near BC, G_{exp} becomes linearly proportional to Δf as indicated by the red dashed line. The previous study revealed that interfacial thermal conductance is linearly proportional to the normal contact force in the BC regime [26], suggesting that Δf can be interpreted as the indicator of the normal force. Therefore, the observed linear relationship between G_{exp} and Δf in the NC regime provides another evidence regarding the existence of forces that induce acoustic phonon transport across vacuum gaps.

Conclusions

In summary, we have conducted comprehensive experiments of thermal transport between Si and Pt surfaces from single-digit nanometre vacuum gap distances to bulk contact, demonstrating force-induced acoustic phonon transport as the mechanism bridging near-field radiation and contact phonon conduction. Excellent agreement between the experimental data and rigorous heat transfer calculations based on the AGF and FE frameworks provides convincing evidence that the observed acoustic phonon transport is due to various force interactions between terminating atoms separated by vacuum. This finding sheds light on the possibility of engineering interfacial thermal transport using external force stimuli, which can impact the development of next-generation thermal management technologies.

Acknowledgements

This work was supported by the National Science Foundation (CBET-1605584) and the Nano Material Technology Development Program (2015M3A7B7045518) through the National Research Foundation of Korea (NRF). A.J. acknowledges financial supports from the University of Utah's Sid Green Fellowship and the National Science Foundation Graduate Research Fellowship (No. 2016213209). T.T. acknowledges financial support from the Sakata Scholarship Foundation. C.S. acknowledges support from the National Science Foundation Graduate Research Fellowship (No. 2017249785). The support and resources from the Center for High Performance Computing at

the University of Utah for AGF calculations are gratefully acknowledged. 3D schematics were generated using the open-source software POV-ray (www.povray.org).

Author Contributions

K.P. and M.F. developed the research idea and directed the project. A.J., J.C., and C.S. designed and conducted the experiments and analyzed the measurement data. T.T. conducted the AGF, FE and DFT calculations and worked with A.J. to compare the measurement and computation results. J.Y. and I.P. fabricated the nanoheater devices for the study, and A.J. and R.M. developed the high-vacuum shear force microscope. A.J., T.T., M.F. and K.P. co-wrote the manuscript with contributions of all authors in discussion.

References

[1] Fiorino, A. *et al.* A Thermal Diode Based on Nanoscale Thermal Radiation. *ACS Nano* **12**, 5774–5779 (2018).

[2] Zhu, L. *et al.* Near-field photonic cooling through control of the chemical potential of photons. *Nature* **566**, 239–244 (2019).

[3] Fiorino, A. *et al.* Nanogap near-field thermophotovoltaics. *Nature Nanotechnology* **13**, 806–811 (2018).

[4] Albisetti, E. *et al.* Nanopatterning reconfigurable magnetic landscapes via thermally assisted scanning probe lithography. *Nature Nanotechnology* **11**, 545–551 (2016).

[5] Rousseau, E. *et al.* Radiative heat transfer at the nanoscale. *Nature Photonics* **3**, 514–517 (2009).

[6] Shen, S., Narayanaswamy, A. & Chen, G. Surface phonon polaritons mediated energy transfer between nanoscale gaps. *Nano Letters* **9**, 2909–2913 (2009).

[7] Song, B. *et al.* Enhancement of near-field radiative heat transfer using polar dielectric thin films. *Nature Nanotechnology* **10**, 253–258 (2015).

[8] St-Gelais, R., Zhu, L., Fan, S. & Lipson, M. Near-field radiative heat transfer between parallel structures in the deep subwavelength regime. *Nature Nanotechnology* **11**, 515–519 (2016).

[9] Bernardi, M. P., Milovich, D. & Francoeur, M. Radiative heat transfer exceeding the blackbody limit between macroscale planar surfaces separated by a nanosize vacuum gap. *Nature Communications* **7**, 12900 (2016).

[10] Song, B. *et al.* Radiative heat conductances between dielectric and metallic parallel plates with nanoscale gaps. *Nature Nanotechnology* **11**, 509–514 (2016).

[11] Watjen, J. I., Zhao, B. & Zhang, Z. M. Near-field radiative heat transfer between doped-Si parallel plates separated by a spacing down to 200 nm. *Applied Physics Letters* **109**, 203112 (2016).

[12] Ghashami, M. *et al.* Precision Measurement of Phonon-Polaritonic Near-Field Energy Transfer between Macroscale Planar Structures Under Large Thermal Gradients. *Physical Review Letters* **120**, 175901 (2018).

[13] Lim, M., Song, J., Lee, S. S. & Lee, B. J. Tailoring near-field thermal radiation between metallo-dielectric multilayers using coupled surface plasmon polaritons. *Nature Communications* **9**, 4302 (2018).

[14] Kim, K. *et al.* Radiative heat transfer in the extreme near field. *Nature* **528**, 387–391 (2015).

[15] Altfeder, I., Voevodin, A. A. & Roy, A. K. Vacuum Phonon Tunneling. *Physical Review Letters* **105**, 166101 (2010).

[16] Kittel, A. *et al.* Near-Field Heat Transfer in a Scanning Thermal Microscope. *Physical Review Letters* **95**, 224301 (2005).

[17] Kloppstech, K. *et al.* Giant heat transfer in the crossover regime between conduction and radiation. *Nature Communications* **8**, 14475 (2017).

[18] Cui, L. *et al.* Study of radiative heat transfer in Ångström- and nanometre-sized gaps. *Nature Communications* **8**, 14479 (2017).

[19] Prunnila, M. & Meltaus, J. Acoustic phonon tunneling and heat transport due to evanescent electric fields. *Physical Review Letters* **105**, 125501 (2010).

[20] Sellan, D. P. *et al.* Phonon transport across a vacuum gap. *Physical Review B* **85**, 024118 (2012).

[21] Ezzahri, Y. & Joulain, K. Vacuum-induced phonon transfer between two solid dielectric materials: Illustrating the case of Casimir force coupling. *Physical Review B* **90**, 115433 (2014).

[22] Chiloyan, V., Garg, J., Esfarjani, K. & Chen, G. Transition from near-field thermal radiation to phonon heat conduction at sub-nanometre gaps. *Nature Communications* **6**, 6755 (2015).

[23] Pendry, J. B., Sasihithlu, K. & Craster, R. V. Phonon-assisted heat transfer between vacuum-separated surfaces. *Physical Review B* **94**, 075414 (2016).

[24] Jarzembski, A. *et al.* Feedback control of local hotspot temperature using resistive on-substrate nanoheater/thermometer. *Review of Scientific Instruments* **89**, 064902 (2018).

[25] Polder, D. & Van Hove, M. Theory of radiative heat transfer between closely spaced bodies. *Physical Review B* **4**, 3303–3314 (1971).

[26] Gotsmann, B. & Lantz, M. A. Quantized thermal transport across contacts of rough surfaces. *Nature Materials* **12**, 59–65 (2013).

[27] Karrai, K. & Tiemann, I. Interfacial shear force microscopy. *Physical Review B* **62**, 13174–13181 (2000).

[28] Edalatpour, S. & Francoeur, M. Near-field radiative heat transfer between arbitrarily shaped objects and a surface. *Physical Review B* **94**, 045406 (2016).

[29] Jarzembski, A. & Park, K. Finite dipole model for extreme near-field thermal radiation between a tip and planar SiC substrate. *Journal of Quantitative Spectroscopy and Radiative Transfer* **191**, 67–74 (2017).

[30] Sadasivam, S. *et al.* The atomistic green's function method for interfacial phonon transport. *Annual Review of Heat Transfer* **17**, 89–145 (2014).

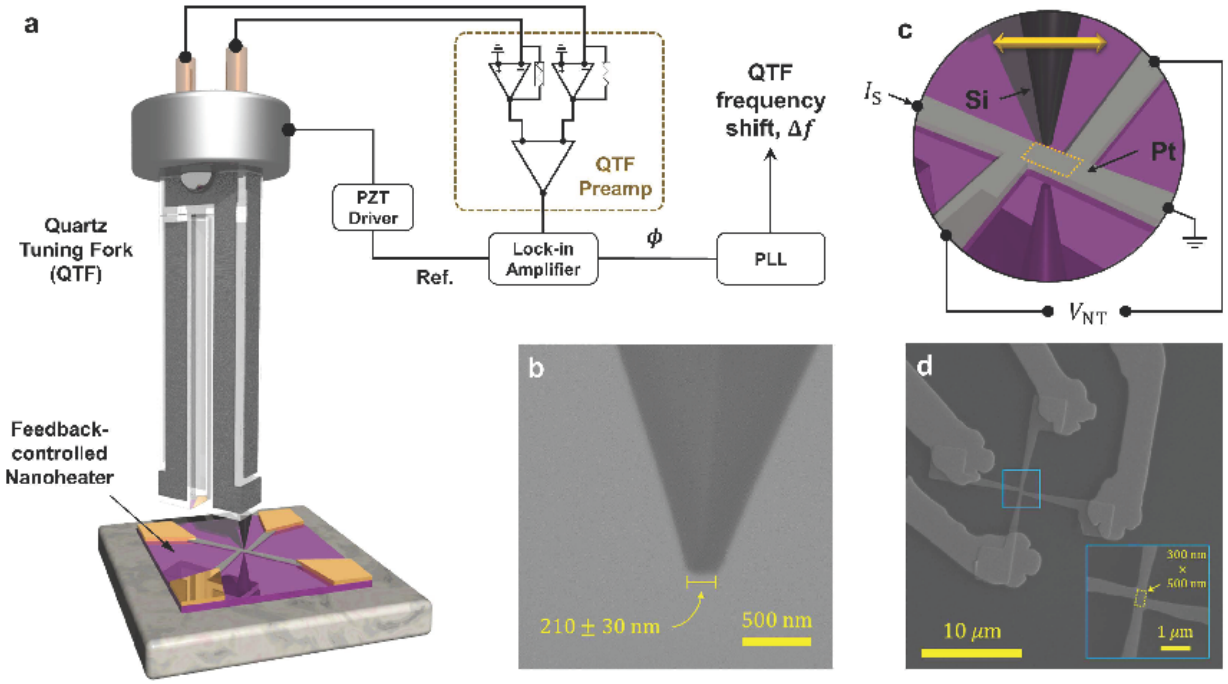

Figure 1: | **Experimental schematic and SEM images of the tip and nanoheater. a,** Experimental schematic based on a custom-built HV-SFM and on-substrate Pt nanoheaters. **b,** SEM image of the Si tip, which exhibits a flat top geometry whose width is 210 ± 30 nm. **c,** Electrical schematic of the nanoheater 4-probe detection scheme with a laterally-oscillating Si tip in close proximity. **d,** SEM images of the nanoheater device showing its maximum sensing area size of 300 nm $\times$ 500 nm (inset).

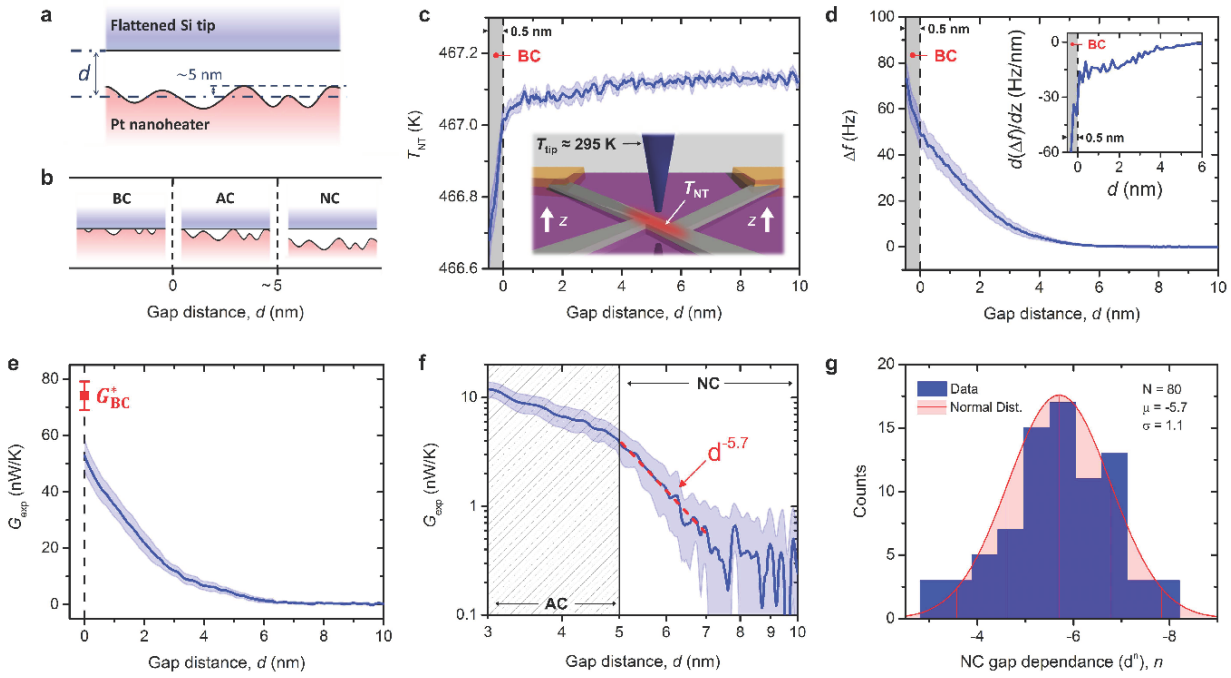

Figure 2: | **Measurement of gap-dependent thermal transport. a,** Illustration of the gap distance (d) defined between the flattened Si tip and the mean line of the nanoheater surface roughness profile. The nanoheater was measured to have a nominal peak-to-peak surface roughness of $\pm$5 nm within at 98.5% confidence interval. **b,** Three regimes defined based on the gap distance, i.e., bulk-contact (BC), asperity-contact (AC), and near-contact (NC). **c,** Feedback-controlled T_{NT} trace as the nanoheater is approached to the tip at room temperature (i.e., $T_{\mathrm{tip}} \approx 295$ K).**d,** Measured Δf of the QTF, illustrating the monotonic increase of tip-sample lateral forces with decreasing d. At BC, this variation becomes more rapid as denoted by its z-derivative drop at 0 nm (inset). **e,** Measured thermal conductance (G_{exp}) as d is reduced to BC. **f,** The result is replotted on a log-log scale to show the gap dependence in the NC regime. In (**c-f**), the solid lines show the average of 13 measurements whose 95% confidence interval is denoted by the blue shaded region. **g,** The distribution of the NC gap dependence (d^n) from 80 measurements, demonstrating its repeatibility at n = -5.7 $\pm$ 1.1.

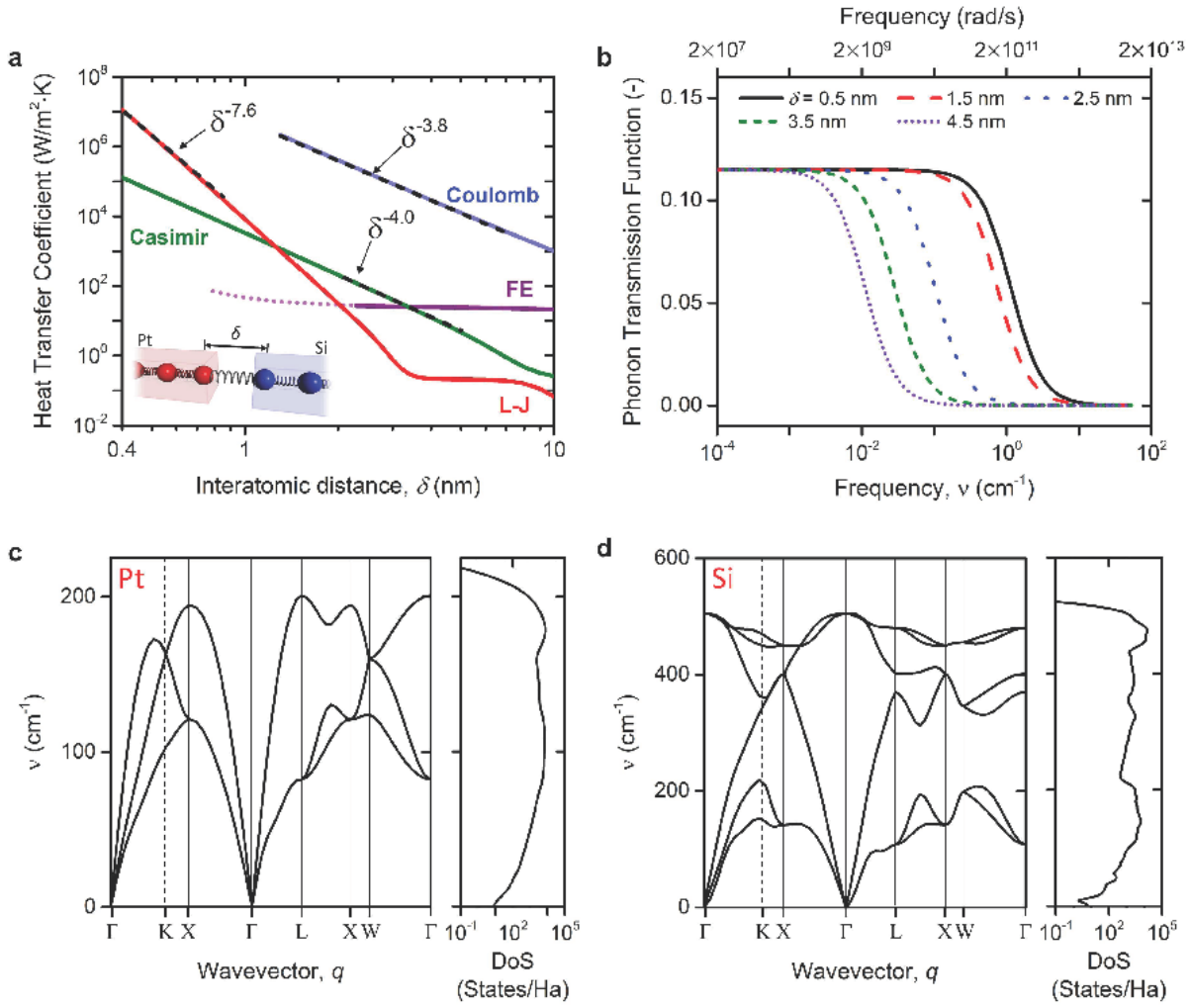

Figure 3: | **Thermal transport calculations by AGF and FE, and phonon dispersion relation and DoS by DFT. a,** Theoretical heat transfer coefficient for varying interatomic distance (δ) computed by AGF and FE, where individual AGF contributions are given by the L-J, Casimir, and Coulomb forces. The possible inaccuracy of FE predictions for $\delta < 2$ nm is emphasized via a dotted line. **b,** Phonon transmission function through the vacuum space calculated by the AGF method. **c,d,** Phonon dispersion relation and DoS calculated by DFT for bulk Pt and Si, respectively. Only acoustic phonons are shown for bulk Pt, while acoustic and optical phonons are plotted for bulk Si. The acoustic-optic crossing value for Si is $\sim$355 cm^{-1}.

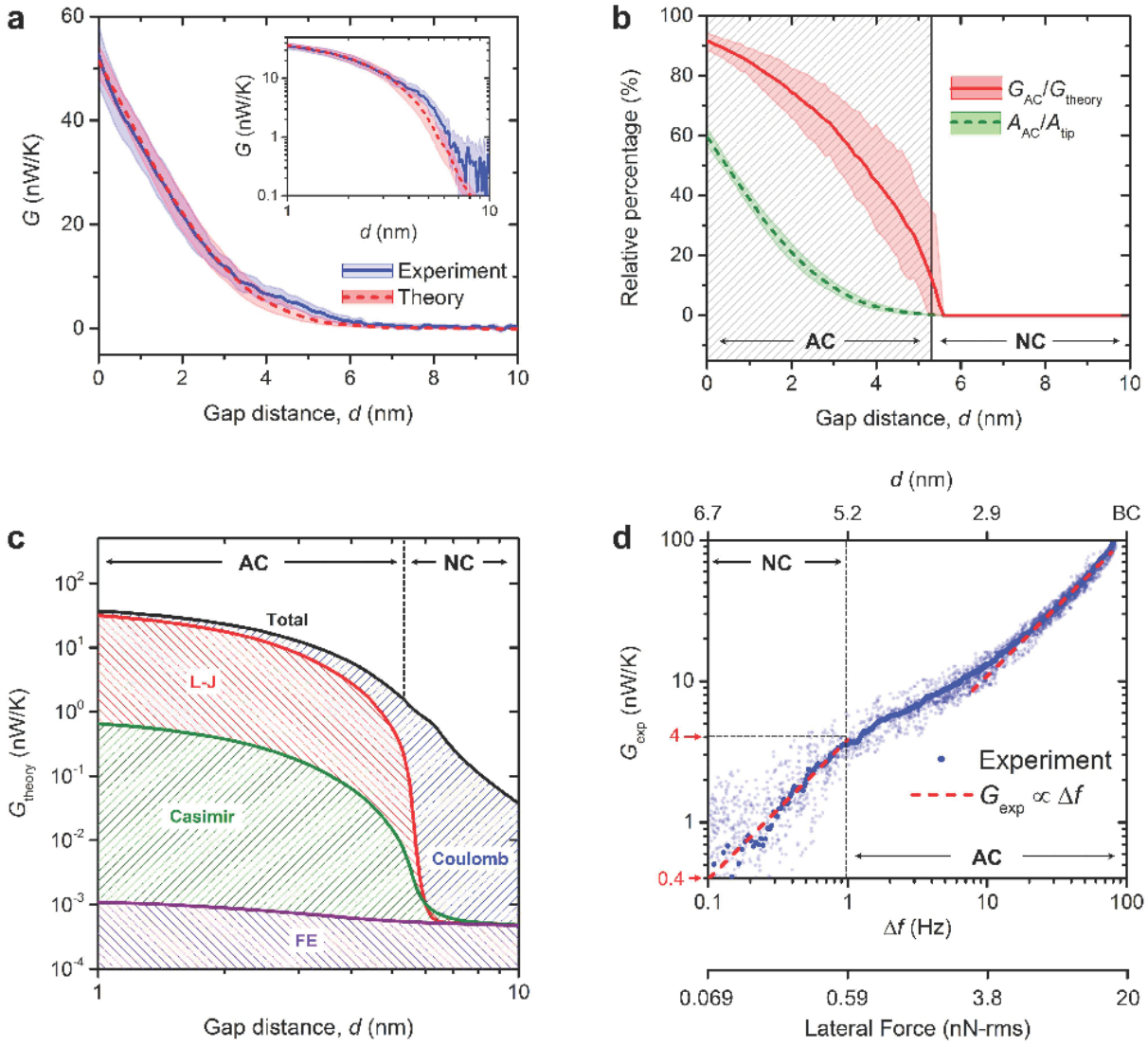

Figure 4: | **Comparison between experiments and theoretical predictions. a,** The theoretical and experimental thermal conductances on linear-linear and (inset) log-log scales. **b,** Calculated AC thermal conductance ratio ($G_{\mathrm{AC}}/G_{\mathrm{theory}}$, where $G_{\mathrm{theory}} = G_{\mathrm{NC}} + G_{\mathrm{AC}}$) and asperity contact ratio ($A_{\mathrm{AC}}/A_{\mathrm{tip}}$), showing the transition between the NC and AC regimes. **c,** AGF force model contributions to G_{theory} compared with FE. **d,** G_{exp} correlation with the simultaneously acquired Δf, where Δf is related to the tip-sample lateral force. The bold lines (red and green) in (**a,b**) show the average value of simulations based on 30 randomly determined rough surfaces whose 95% confidence interval is denoted by the shaded region.

Methods

High-vacuum shear force microscopy (HV-SFM)

QTF-based SFM is an AFM modality that uses a vertically aligned QTF resonator as a probe instead of a cantilever (Fig. 1a). The QTF has a tip mounted to one of its tines, which interacts with the surface to generate nanoscale topographic images [31]. The HV-SFM used in this work is a custom-built, high vacuum system (5×10^{-6} Torr in routine operations) interfaced with commercial control electronics (RHK Technology, R9). The piezoelectric sample stage has an *x,y,z*-scanning range of 30 μm $\times$ 30 μm $\times$ 10 μm. In addition, slip-stick piezoelectric motors embedded in the sample stage allows coarse *x,y,z*-motion with a range of 5 mm $\times$ 5 mm $\times$ 10 mm. The sample stage is equipped with 16-pin electrical feedthroughs for electric connections for vacuum experiments. When the QTF is mechanically driven at its in-plane anti-phase resonant frequency (f_0 = 32.768 kHz), the oscillation of the QTF tines generates a piezoelectric current [27]. The QTF signal, which is pre-amplified with a gain of 10^9 V/A in the SFM head, is processed by a lock-in amplifier and phase-locked-loop (PLL) to real-time monitor the QTF resonance frequency shift (i.e., $\Delta f = f - f_0$) for SFM imaging.

Z-piezo calibration of the HV-SFM sample stage. In order to accurately calibrate the vertical displacement of the piezo-actuated sample stage, we measure the Δz-sensitivity of the sample stage by implementing optical fiber interferometry (OFI). Fig. 5a shows the schematic of the OFI at the operating wavelength of λ = 1310 nm, configured on top of the sample stage. For calibration, a gold (Au) retroreflector is mounted on the stage. The fiber orientation is then aligned to make normal light incidence to the Au retroreflector surface. After interaction with the fiber-sample junction, the reflected signals are directed towards a photodetector (Femto, OE-200-IN1). As shown in Fig. 5a', a Fabry-Pérot cavity is formed between the fiber-air interface (ray 1) and the Au retroreflector (ray 2), yielding the OFI signal highly sensitive to the Δz-motion of the sample stage [32]. A photograph of the OFI setup is shown in Figs. 5b,c.

The first step is to calibrate the OFI sensitivity by correlating the optical fiber signal (V_{OFI}) to vertical displacement of the fiber aperture. After the initial alignment of the optical fiber, the Fabry-Pérot interference fringes are measured as the piezo-actuator (i.e., fiber piezo) slowly moves the fiber aperture down to the fixed Au retroreflector. As shown in Fig. 5d, the vertical displacement of the fiber aperture by λ/4 (i.e., 327.5 nm) should yield half a period of V_{OFI} oscillation due to optical interference between ray 1 and ray 2 at the fiber aperture. When the fiber aperture position slightly changes around the mid-fringe value at V_{OFI} = 5 V (red dot), V_{OFI} can be approximated to be linearly proportional to the fiber piezo voltage with a sensitivity of $\Delta V_{\mathrm{OFI}}/\Delta V_{\mathrm{FP}}$ = 3.97 V/V. Thus, the OFI sensitivity (β_{OFI}) can be defined as:

$$\frac{1}{\beta_{\mathrm{OFI}}} = \frac{\Delta V_{\mathrm{FP},\lambda/4}}{\lambda/4}\frac{\Delta V_{\mathrm{OFI}}}{\Delta V_{\mathrm{FP}}}, \tag{1}$$

where $\Delta V_{\mathrm{FP},\lambda/4}$ = 2.21 V is the fiber piezo voltage required to move the fiber position by λ/4 . For our setup, β_{OFI} is determined to be 37.3 nm/V.

Once β_{OFI} is determined, the Δz-motion of the sample stage can be optically calibrated by $\Delta z = \beta_{\mathrm{OFI}}\Delta V_{\mathrm{OFI}}$. Fig. 5e presents the Δz-motion measured by the OFI as the z-piezo voltage of the sample stage is varied by $\Delta V_{\mathrm{z}} = \pm 1$ V about the center position at which the optical fiber aperture is initially positioned at $V_{\mathrm{OFI}} = 5$ V. The 95% confidence interval of 20 measurements (light green) and their average (dark green) show linear motion of the sample stage. From these measurements, the z-piezo sensitivity about its center position is determined to be $\beta_{\mathrm{z}} = \Delta z/\Delta V_{\mathrm{z}} = 28.0 \pm 2.8$ nm/V. To verify the calibrated Δz-sensitivity, we conducted HV-SFM imaging of a 6H-SiC half-monolayer sample whose steps are well defined as 7.5 Å (K-Tek Nanotechnology, SiC/0.75). As shown in Figs. 5f,g, the calibrated Δz-sensitivity (i.e., $\beta_{\mathrm{z}} = 28.0$ nm/V) yields the accurate half-monolayer height of 6H-SiC in the HV-SFM image. From the statistical analysis of the obtained 6H-SiC half-monolayer topographic image, the z-position uncertainty of the sample stage is estimated to be 1.8 Å .

Preparation and Characterization of QTF probes

The QTF probes are prepared by attaching a commercial microcantilever with a silicon tip (Bruker, FMV-A) to the free end of a QTF tine. The tip attaching process is illustrated in Fig. 6a. While the bare QTF (i.e., with shielding removed) is fixed with its tines oriented vertically, a small amount of UV curable epoxy (Bondic) is deposited on the free end of one QTF tine by a needle attached to a 3-axis micropositioner (Step 1). The microcantilever is then adhered to the epoxy droplet (Step 2), followed by UV curing of the epoxy to form a cold weld of the cantilever (Step 3). Lastly, by pushing the entire chip down with the micropositioner, only the cantilever is left adhered on the QTF end (Step 4). Figs. 6b-c show optical microscope images of the resulting QTF with Si tip, which was used to perform the measurements in Figs. 2c-f. It should be noted that the tip is rigidly adhered to the QTF thus preventing any snap-in artifact.

Calibration of the QTF oscillation amplitude. In order to minimize any effect of lateral tip motion onto the tip-nanoheater thermal transport measurement, the QTF oscillation amplitude is maintained within the sub-nanometre range. The oscillation amplitude of a QTF probe was measured with the same OFI system described previously, where β_{OFI} was recalibrated to 50.0 nm/V to accommodate the less reflective QTF surface. As illustrated in Fig. 7a, the optical fiber aperture is aligned to a reflective portion of the tip-attached QTF tine a distance z_{m} away from its base. Both the electrical outputs from the QTF and OFI are then simultaneously demodulated at the QTF resonant frequency to correlate the lateral oscillation amplitude of the tip (Δx_{tip}) with the QTF electrical signal (Δx_{e}). It should be noted that the geometry of the QTF is used to linearly relate the measured oscillation amplitude at z_{m} (i.e., Δx_{m}) to the tip motion at z_{tip}. The calibration result is shown in Fig. 7b, where the QTF amplitude signal sensitivity is determined to be $\alpha = 7.32 \pm 0.05$ pm/mV. The QTF electrical signal was set to $\sim$70 mV-rms at its resonance frequency ($f_0 = 32.768$ kHz) during experiments, which corresponds to a lateral tip motion of $\sim$500 pm-rms. This tip motion is on the order of the average lattice constant of the Si-Pt system [33, 34] and is approximately three orders of magnitude smaller than the effective surface area subjected to thermal transport. We believe that such small lateral tip oscillation would not affect our thermal transport measurement.

Quantification of the tip-sample conservative lateral force using the HV-SFM. The working principle of HV-SFM is the force interaction between a laterally oscillating tip and underlying sample surface. Therefore, the lateral force exerted on the tip can be experimentally detected by monitoring the QTF's Δf. Using the first-order QTF oscillator model, the conservative lateral force parallel to the sample surface (F_x) is linearly proportional to Δf and can be written as [35]:

$$F_x = \frac{2k_{\mathrm{eff}}\Delta x_{\mathrm{tip}}}{f_0}\Delta f. \tag{2}$$

The effective spring constant, k_{eff}, can be approximated as $k_{\mathrm{eff}} \approx Ewt^3/(4l^3)$, where $E = 7.87 \times 10^{10}$ N/m^2 is the Young's modulus of quartz [36]. Using the dimensions of the QTF tine ($l = 3.52$ mm; $w = 0.25$ mm; $t = 0.58$ mm), k_{eff} is estimated to be 22.0 kN/m.

Measurement of Si-Pt bulk-contact thermal conductance

To fully understand the transition from near-contact (NC) to bulk-contact (BC) thermal transport, the tip should approach the nanoheater sensing region to form BC while avoiding damage to the tip and nanoheater. However, the high vertical rigidity of the QTF can easily damage both the tip and nanoheater when the tip is further pushed once BC is made. To address this challenge, we conducted BC measurements separately by using a cantilever in high vacuum (Fig. 8a). It should be noted that our HV-SFM also has a regular AFM head for cantilever-based operations. The cantilever used in the bulk-contact experiments is the same model (Bruker, FMV-A) as was mounted to the QTFs for the near-contact measurements. Detection of the cantilever deflection is achieved by an optical fiber interferometer aligned with the cantilever's backside [32]. Nanoheater #2 was used for the BC measurement (topography shown in Fig. 8b), whose sensing area is 330 nm $\times$ 375 nm in size (red dashed rectangle). The calibration data of nanoheater #2 can be found in the Supplementary Section 1. After AFM topographic imaging with soft-contact mode ($F_{\mathrm{z}} \lesssim 3$ nN), the BC measurement was conducted by approaching the nanoheater to the tip until they make hard contact. An SEM image of the Si tip after the BC measurements is shown in Fig. 8c. During hard contact ($F_{\mathrm{z}} \gtrsim 15$ nN), we believe that bulk contact is made at the flattest portion of the tip apex whose contact diameter is 215$\pm$25 nm (inset).

For both the cantilever- and QTF-based experiments, the nanoheater current, I_{S}, was monitored using an in-series current preamplifier (Femto, DLPCA), while the voltage drop across the sensing region, V_{NT}, was measured using a differential voltage amplifier (SRS, SR640). The nanoheater sensing region resistance was digitally computed and feedback-controlled by the AFM controller. The only difference in the cantilever-based measurements is that after snap-in-contact is made, the cantilever is further pushed to achieve BC between the tip and nanoheater. Fig. 8d presents the cantilever deflection and T_{NT} signals as a function of the tip position. At a distance of 5 nm, the cantilever snaps into contact as denoted by the sudden drop of the cantilever deflection and T_{NT}. As the tip is continuously pushed toward the nanoheater, the cantilever returns to its neutral position, which is referred to as the zero z-displacement position [14]. In the negative displacement regime, the sample pushes the cantilever to bend backwards such that bulk contact is made with a sufficient contact force. Meanwhile, the feedback controller settles T_{NT} to the setpoint by increasing the heating power. Fig. 8e shows the corresponding value of G_{exp}, which remains zero in the gap region, rapidly increases at snap-in, and gradually increases as the cantilever is further pushed. The gradual increase of the thermal conductance is indicative of the onset of bulk contact and is attributed to the pressure dependence of the interfacial thermal resistance [26]. From this measurement, the BC thermal conductance (G_{BC}) between the Si tip and Pt nanoheater is determined to be 121.9 $\pm$ 8.4 nW/K at the z-displacement of -5 nm, where T_{NT} returns to the setpoint and the contact force is $\sim$15 nN. For proper comparison with the QTF-based experiments, the obtained G_{BC} is adjusted by considering the different effective contact areas. The adjusted thermal conductance, G^*_{BC}, is estimated to be 74.1 $\pm$ 5.1 nW/K and is shown in Fig. 8e.

Surface cleaning and characterization of tip and nanoheater

To ensure that the interacting surfaces are free from contamination prior to experiments, a routine surface inspection and cleaning protocol was established for the QTF probes and nanoheaters. First, several QTF probes and nanoheaters are inspected using SEM to select the ones with no major debris around the sensing areas (Figs. 1b,d). After initial sonication cleaning with acetone, they are placed inside of a deep ultraviolet (UV) ozone cleaner (Novascan, PSD-UV4) chamber located in a class-1000 modular cleanroom to remove organic contamination using UV wavelengths at 185 and 254 nm [37]. The UV-ozone cleaner is set to generate ozone for 2 hours. After treatment, the QTF probe and the nanoheater are promptly mounted to the HV-SFM, and the chamber is evacuated to high vacuum to minimize undesired exposure to the ambient before experiments [18]. Moreover, all experiments were carried out at high temperature (i.e., 467 K), which inherently removes weakly bonded contaminants from the surface.

In order to secure a sufficient heat transfer area, the Si tip was flattened by long-line scanning on the nanoheater substrate (i.e., a 500-nm thick silicon nitride film on top of a silicon substrate) at a contact force of $\sim$10 nN. Once the flattened tip was attached to the QTF, we conducted long-line shear force scanning on the nanoheater substrate in the AC regime for the fine adjustment of surface parallelism. Since the nanoheater surface profile plays a pivotal role in determining different contact regimes, we acquired the nominal surface roughness distribution of the nanoheater sensing region by soft-contact AFM imaging (e.g., Fig. 8b). A small contact force ($\lesssim$ 3 nN) during the AFM imaging results in a contact diameter of $\sim$ 8 nm as estimated by the Hertzian model [38]. A surface roughness histogram of the nanoheater sensing region from the obtained AFM image shows a Gaussian distribution centered at 0 nm with a standard deviation of $\sigma = 1.96$ nm (Fig. 9a). The equivalent peak roughness $\mathrm{SR_p}$ is approximately 5 nm within a 98.5% confidence interval (Fig. 2a). The Gaussian distribution of the surface roughness is used to randomly regenerate a nanoheater surface for AGF calculations (Fig. 9b).

Calculation of theoretical thermal conductance

The theoretical thermal conductance, G_{theory}, is calculated by considering the heat transfer coefficients due to force-induced acoustic phonon and radiation transport combined with the Derjaguin approximation based on the measured surface roughness of the Pt nanoheater [39]. Although the heat transfer coefficient due to electron tunneling is also calculated based on the ideal assumption as described in Supplementary Section 7, its contribution turns out to be orders of magnitudes smaller than the other mechanisms and thus is not included here. Throughout the following discussion, the subscripts L and R refer to the left and right regions that are respectively made of Pt and Si (Fig. 10a). The temperatures of the left and right regions are fixed at T_{L} = 470 K and T_{R} = 300 K.

Force-induced acoustic phonon heat transfer coefficient. The heat flux due to force-induced acoustic phonon transport across the interatomic vacuum distance δ for the 1D atomic chain shown in Fig. 10a is given by [30]:

$$q_{\mathrm{ph}} \;=\; \frac{1}{A_{\mathrm{Si-Pt}}}\int_0^\infty d\omega \frac{\hbar\omega}{2\pi}\mathcal{T}_{\mathrm{ph}}(\omega)[N(\omega,T_{\mathrm{L}}) - N(\omega,T_{\mathrm{R}})] \tag{3}$$

where $N = 1/[\exp(\hbar\omega/k_{\mathrm{b}}T) - 1]$ is the Bose-Einstein distribution function. The effective heat transfer area, $A_{\mathrm{Si-Pt}}$, is the projected atomic area calculated using an average atomic radius:

$$A_{\mathrm{Si-Pt}} \;=\; \pi\left(\frac{r_{\mathrm{Pt}} + r_{\mathrm{Si}}}{2}\right)^2 \tag{4}$$

where $r_{\mathrm{Pt}} = 1.77{\times}10^{-12}$ m and $r_{\mathrm{Si}} = 1.11{\times}10^{-12}$ m are the atomic radius of Pt and Si, respectively [40]. The phonon transmission function, $\mathcal{T}_{\mathrm{ph}}$, is derived from the atomistic Green's function (AGF) method [30]. In this framework, Pt and Si are modeled as semi-infinite leads separated by a device region containing atoms of Pt and Si separated by the vacuum region. The phonon transmission function is written as:

$$\mathcal{T}_{\mathrm{ph}}(\omega) \;=\; \mathrm{Trace}[\Gamma_{\mathrm{L}} G_{\mathrm{d}} \Gamma_{\mathrm{R}} G_{\mathrm{d}}^{\dagger}] \tag{5}$$

where the superscript † denotes conjugate transpose. The escape rate of phonons from the device region to the semi-infinite leads, $\Gamma_{\mathrm{L,R}}$, is defined as:

$$\Gamma_{\mathrm{L,R}} = i[\Sigma_{\mathrm{L,R}} - \Sigma_{\mathrm{L,R}}^{\dagger}] \tag{6}$$

where $\Sigma_{\mathrm{L,R}}$ is the self-energy matrix:

$$\Sigma_{\mathrm{L,R}} = \tau_{\mathrm{L,R}} g_{\mathrm{L,R}} \tau_{\mathrm{L,R}}^{\dagger} \tag{7}$$

In Eq. (7), $\tau_{\mathrm{L,R}}$ is the matrix connecting the left (L) or right (R) semi-infinite lead to the device region. The connection matrix is computed via the force constant between the atoms bounding the semi-infinite leads and the device region, and

the atomic masses. The atomic masses of Pt and Si are 3.239×10^{-25} kg and 4.664×10^{-26} kg, respectively [41]. The term $g_{\mathrm{L,R}}$ is the uncoupled Green's function (also called surface Green's function) derived from the harmonic matrix of the left (L) or right (R) semi-infinite lead. The uncoupled Green's function is computed using the decimation technique described in Ref. [30]. The device Green's function, G_{d}, needed to calculate the phonon transmission function is given by:

$$G_{\mathrm{d}} \;=\; \left[\omega^2 I - H_{\mathrm{d}} - \Sigma_{\mathrm{L}} - \Sigma_{\mathrm{R}}\right]^{-1} \tag{8}$$

where I is the identity matrix, and H_{d} is the harmonic matrix of the device region. Heat transfer due to acoustic phonon transport between Pt and Si is mediated by short-range and long-range forces in the vacuum region; short- and long-range force constants are included in the matrix H_{d}. In this work, the Lennard-Jones (L-J), Casimir, and Coulomb forces connect the Pt and Si atomic chains. The rational behind this choice and details regarding calculation of force constants acting in the vacuum region are provided in Supplementary Section 5.

The heat transfer coefficient due to force-induced acoustic phonon transport is obtained by dividing the heat flux by the temperature difference ΔT ($= T_{\mathrm{L}} - T_{\mathrm{R}}$), i.e., $h_{\mathrm{ph}} = q_{\mathrm{ph}}/\Delta T$. Fig. 3a shows the individual contribution of the L-J, Casimir, and Coulomb forces to the force-induced acoustic phonon heat transfer coefficient. Note that five atoms of Pt and five atoms of Si in the device region are sufficient to obtain stable and converged results.

Radiative heat transfer coefficient. Radiative heat transfer is calculated using fluctuational electrodynamics (FE) [42]. The radiative flux is given by:

$$q_{\mathrm{rad}} \;=\; \frac{1}{\pi^2}\int_0^\infty d\omega \left[\Theta\left(\omega, T_{\mathrm{L}}\right) - \Theta\left(\omega, T_{\mathrm{R}}\right)\right] \int_0^\infty dk_\rho k_\rho \sum_{p=\mathrm{TE,TM}} \mathcal{T}^p_{\mathrm{rad}}\left(\omega, k_\rho\right) \tag{9}$$

where ω is the angular frequency, and k_ρ is the component of the wavevector parallel to an interface. $\Theta(\omega, T)$ is the mean energy of an electromagnetic state calculated as $\hbar\omega/[\exp(\hbar\omega/k_{\mathrm{b}}T) - 1]$, where $\hbar$ is the reduced Planck constant and k_{b} is the Boltzmann constant. For two infinite planes separated by an interatomic vacuum distance $\bar{\delta}$, the transmission functions in polarization state p (TM and TE) for propagating ($k_\rho < k_0$) and evanescent ($k_\rho > k_0$) waves in vacuum are respectively given by [25]:

$$\mathcal{T}^p_{\mathrm{rad,prop}}\left(\omega, k_\rho\right) \;=\; \frac{\left(1 - \left|r^p_{0\mathrm{L}}\right|^2\right)\left(1 - \left|r^p_{0\mathrm{R}}\right|^2\right)}{4\left|1 - r^p_{0\mathrm{L}} r^p_{0\mathrm{R}} e^{2i\mathrm{Re}(k_{\mathrm{z0}})\bar{\delta}}\right|^2} \tag{10}$$

$$\mathcal{T}^p_{\mathrm{rad,evan}}\left(\omega, k_\rho\right) \;= e^{-2\mathrm{Im}(k_{\mathrm{z0}})\bar{\delta}} \frac{\mathrm{Im}\left(r^p_{0\mathrm{L}}\right)\mathrm{Im}\left(\mathrm{r}^p_{0\mathrm{R}}\right)}{\left|1 - r^p_{0\mathrm{L}} r^p_{0\mathrm{R}} e^{-2\mathrm{Im}(k_{\mathrm{z0}})\bar{\delta}}\right|^2} \tag{11}$$

where the subscript 0 refers to vacuum, k_{z} is the component of the wavevector perpendicular to an interface, and $r^p_{0\mathrm{j}}$ is the Fresnel reflection coefficient at the vacuum/Pt ($j = \mathrm{L}$) or vacuum/Si ($j = \mathrm{R}$) interface in polarization state p. The transmission functions are calculated using the surface-to-surface distance $\bar{\delta} = \delta - r_{\mathrm{Pt}} - r_{\mathrm{Si}}$. The frequency-dependent dielectric functions of Pt and Si needed to calculate the Fresnel coefficients and the perpendicular wavevector are described by the models proposed by Djurisic *et al.* [43] and Adachi *et al.* [44], respectively.

The radiative heat transfer coefficient, h_{rad}, is obtained by $h_{\mathrm{rad}} = q_{\mathrm{rad}}/\Delta T$. For comparison with force-induced acoustic phonon transport in Fig. 3a, the radiative heat transfer coefficient is calculated down to an interatomic vacuum distance δ of 0.8 nm. Since FE is a theory based on the macroscopic Maxwell equations that is unlikely to be valid for such a small distance, the FE results below $\delta = 2$ nm are plotted with a dotted curve. The potential inaccuracy of FE has no impact on the theoretical thermal conductance, G_{theory}, since heat transfer is largely dominated by force-induced acoustic phonon transport for $\delta < 2$ nm. Note that the contribution of optical phonons to heat transport is taken into account within h_{rad} via the dielectric function of the materials [45].

Calculation of theoretical thermal conductance. The Derjaguin approximation [39] is used to calculate the theoretical thermal conductance, G_{theory}, based on the measured nanoheater surface roughness distribution (Figs. 9 and 10b). Specifically, the thermal conductance at a gap d is computed as a summation of local heat transfer coefficient, h_i, between two flat sub-surfaces of Pt and Si separated by a local interatomic distance δ_i:

$$G_{\mathrm{theory}}\left(d\right) = \sum_{i=1}^{N} h_i\left(\delta_i\right) A_i. \tag{12}$$

where N is the number of flat sub-surfaces with area A_i. Discretization into sub-surfaces relies on the surface roughness distribution based on the nominal nanoheater surface profile (Fig. 9a). The minimum value of δ_i (i.e., contact) is set to 4.68 Å, which is the average value of the lattice constants for Pt (3.92 Å) [33] and Si (5.43 Å) [34]. The effective heat

transfer area, limited by the Si tip area, is determined based on the SEM image shown in Fig. 1b. We approximate the Si tip as a flattened square whose diagonal length is 210 nm $\left(\text{i.e., } A_{\text{tip}} = \left(210 \times 10^{-9}/\sqrt{2}\right)^2 = 2.21 \times 10^{-14}\ \text{m}^2\right)$. The underlying nanoheater surface, whose area is the same as A_{tip}, is discretized into N square sub-surfaces of equal size (i.e., $A_i = A_{\text{tip}}/N$). A convergence analysis was performed by discretizing the Pt nanoheater into 100, 1024 and 2500 sub-surfaces; 1024 sub-surfaces were found sufficient to provide converged results. The gap distance d is defined in accordance with Fig. 2a, separating the average value of the Pt nanoheater surface roughness with the flattened Si tip. Therefore, the variation of each nanoheater sub-surface about d is given as $(d - \delta_i)$ for both convex and concave surface features, taking maximum/minimum values of $\sim \pm 5$ nm as shown in Fig. 2a.

The combination of surface roughness distribution and the Derjaguin approximation enables the conversion of the heat transfer coefficient to a theoretical thermal conductance, G_{theory}, that can be quantitatively compared against experimental data (Fig. 4a). Note that to develop statistically relevant theoretical predictions within a 95% confidence interval, Eq. (12) was solved for 30 randomly determined sets of surface roughness distribution resulting in 30 sets of G_{theory}-d curves. In Figs. 4a,b, the bold lines correspond to the average theoretical thermal conductance ($G_{\text{theory}}^{\text{average}}$), while the shaded regions are generated by calculating $G_{\text{theory}}^{\text{average}} \pm 2\sigma$, where σ is the standard deviation.

Phonon dispersion relations and density of states (DoS)

Phonon dispersion relations and DoS of bulk Pt and Si are calculated via the density functional theory (DFT) as implemented in ABINIT (see Figs. 3c,d) [46]. In the DFT calculations, the lattice constants of Pt and Si are defined as 3.92 Å and 5.43 Å , respectively [33, 34]. Plane wave cut-off energies are selected as 35 Hartree (Ha) for Pt [47] and 30 Ha for Si [34] for self-consistent calculations (1 Ha = 4.360×10^{-18} J). The Optimized Norm-Conserving Vanderbilt (ONCV) pseudopotentials [48] is used for Pt and the local density approximation (LDA) [49] based Troullier-Martins pseudopotentials is employed for Si. The first Brillouin zone is sampled with 4×4×4 Monkhorst-Pack grid for both cases.

Methods References

[31] Ko, J., Jarzembski, A., Park, K. & Lee, J. Hydrogel tip attached quartz tuning fork for shear force microscopy. *Micro and Nano Systems Letters* **6**, 8 (2018).

[32] Rugar, D., Mamin, H. J. & Guethner, P. Improved fiber-optic interferometer for atomic force microscopy. *Applied Physics Letters* **55**, 2588–90 (1989).

[33] Feibelman, P. J. *et al.* The CO/Pt(111) Puzzle. *The Journal of Physical Chemistry B* **105**, 4018–4025 (2001).

[34] Esfarjani, K., Chen, G. & Stokes, H. T. Heat transport in silicon from first-principles calculations. *Physical Review B* **84**, 085204 (2011).

[35] Castellanos-Gomez, A., Agrait, N. & Rubio-Bollinger, G. Force-gradient-induced mechanical dissipation of quartz tuning fork force sensors used in atomic force microscopy. *Ultramicroscopy* **111**, 186–190 (2011).

[36] Grober, R. D. *et al.* Fundamental limits to force detection using quartz tuning forks. *Review of Scientific Instruments* **71**, 2776–2780 (2000).

[37] Tsao, C. W., Hromada, L., Liu, J., Kumar, P. & DeVoe, D. L. Low temperature bonding of PMMA and COC microfluidic substrates using UV/ozone surface treatment. *Lab on a Chip* **7**, 499–505 (2007).

[38] Derjaguin, B., Muller, V. & Toporov, Y. Effect of contact deformation on the adhesion of elastic solids. *Journal of Colloid Interface Science* **53**, 314–326 (1975).

[39] Derjaguin, B., Abrikosova, I. & Lifshitz, E. Direct measurement of molecular attraction between. *Quarterly Reviews, Chemical Society* **10**, 295–329 (1956).

[40] Clementi, E., Raimondi, D. L. & Reinhardt, W. P. Atomic screening constants from SCF functions. II. Atoms with 37 to 86 electrons. *The Journal of Chemical Physics* **47**, 1300–1307 (1967).

[41] Meija, J. *et al.* Atomic weights of the elements 2013 (IUPAC Technical Report). *Pure and Applied Chemistry* **88**, 265–291 (2016).

[42] Rytov, S., Kravtsov, Y. & Tatarskii, V. *Principles of Statistical Radiophysics*, vol. 3 (Springer, New York, 1989).

[43] Djurišić, A. B., Elazar, J. M. & Rakić, A. D. Simulated-annealing-based genetic algorithm for modeling the optical constants of solids. *Applied Optics* **36**, 7097 (1997).

[44] Adachi, S. Model dielectric constants of Si and Ge. *Physical Review B* **38**, 12966–12976 (1988).

[45] Messina, R., Biehs, S.-A., Ziehm, T., Kittel, A. & Ben-Abdallah, P. Heat transfer between two metals through subnanometric vacuum gaps. *arXiv* 1–5 (2018). URL `http://arxiv.org/abs/1810.02628`. `1810.02628`.

[46] Gonze, X. *et al.* First-principles computation of material properties: the ABINIT software project. *Computational Materials Science* **25**, 478–492 (2002).

[47] Sun, T., Umemoto, K., Wu, Z., Zheng, J. C. & Wentzcovitch, R. M. Lattice dynamics and thermal equation of state of platinum. *Physical Review B* **78**, 024304 (2008).

[48] Hamann, D. R. Optimized norm-conserving Vanderbilt pseudopotentials. *Physical Review B* **88**, 085117 (2013).

[49] Kohn, W. & Sham, L. J. Self-Consistent Equations Including Exchange and Correlation Effects. *Physical Review* **140**, A1133–8 (1965).

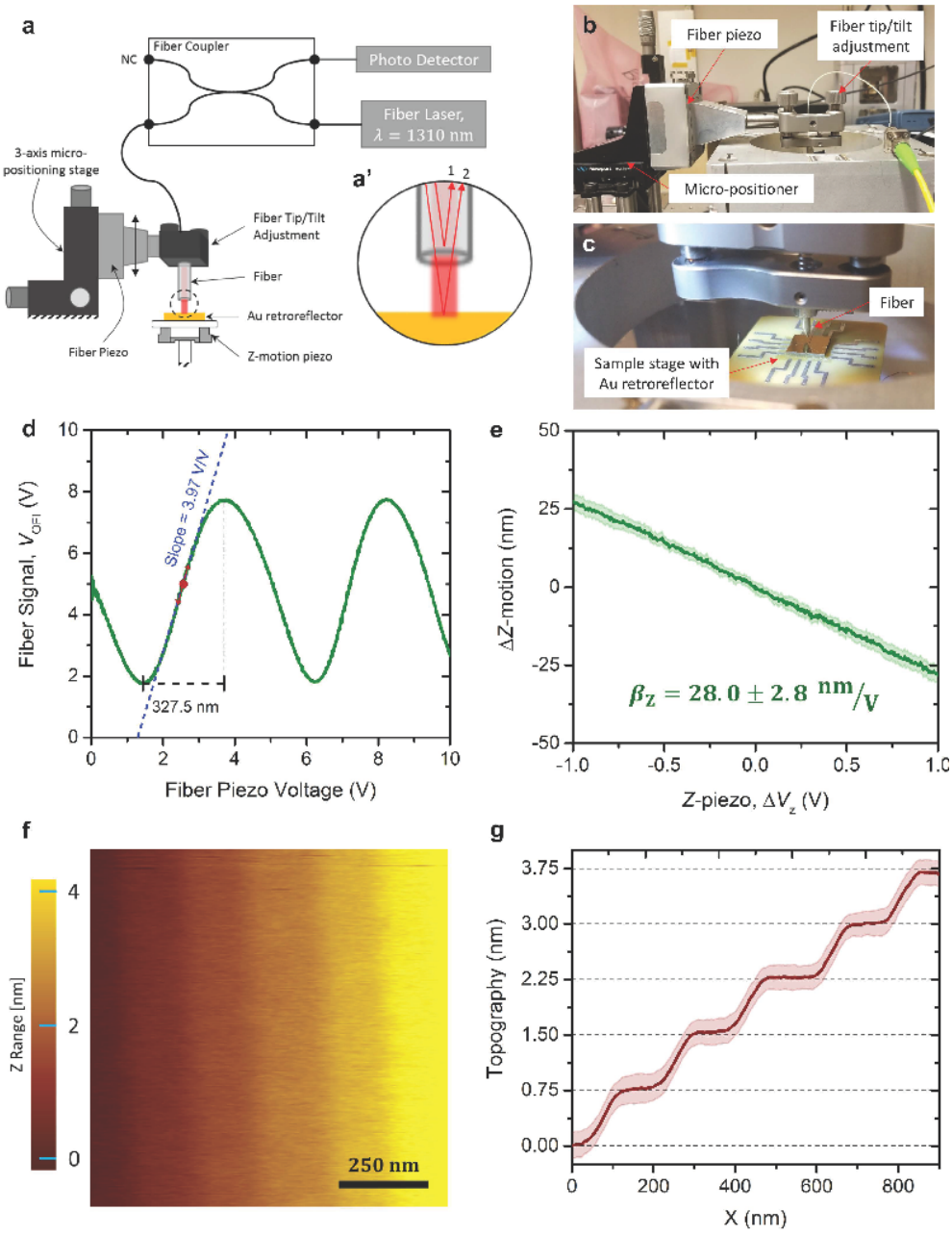

Figure 5: | **Calibration of the SFM z-motion stage. a,** Calibration setup based on an optical fiber interferometer (OFI) with λ = 1310 nm used to calibrate the Δz-motion of the piezo stage. **b,c,** Photographs of the calibration setup. **d,** Interference fringes observed by moving the fiber position with respect to the Au retroreflector. **e,** Δz-motion of the sample stage while actuating the Z-piezo ΔV_z ± 1 V around the experimental position (i.e., piezo center position). Shown is the 95% confidence interval of 20 measurements (light green) and their average (dark green). From this, the z-piezo sensitivity (β_z) is found to be 28.0 $\pm$ 2.8 nm/V. Verification of β_z obtained by performing SFM imaging on a 6H-SiC half-monolayer test sample showing (**f**) topography (256$\times$256 pixels) where 5 half-monolayers are observed. **g,** Statistical line trace, showing that when $\beta_z = 28.0$ nm/V, the half-monolayer thickness corresponds to its expected value of 7.5 Å. The solid red line is the average value of 256 lines where the shaded region represents the $\pm 1\sigma$ uncertainty of 1.8 Å.

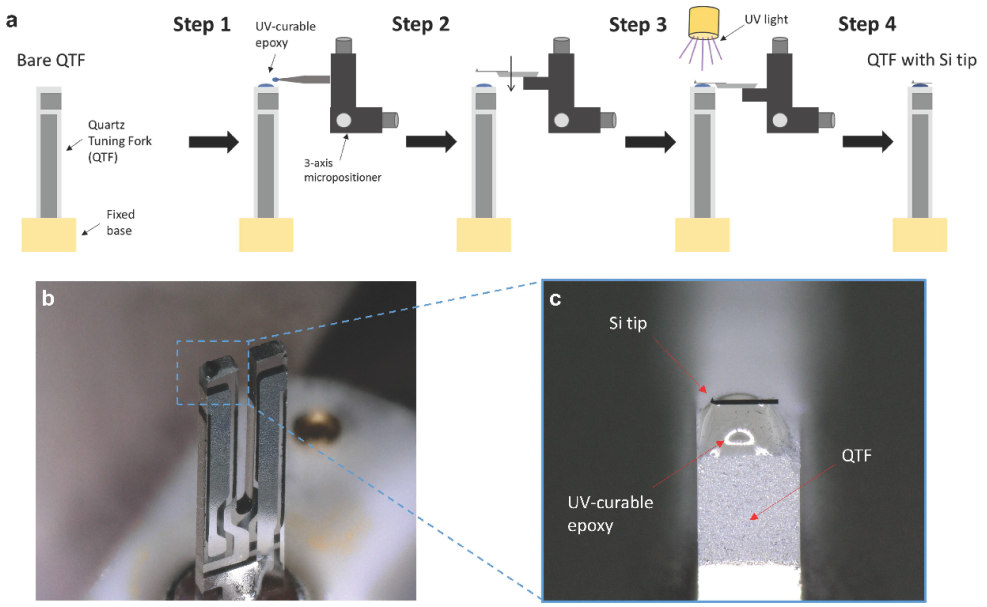

Figure 6: | **Preparation of the QTFs with Si tip. a,** Step-by-step process used to rigidly mount an Si tip to the free end of a QTF using ultraviolet (UV) curable epoxy. **b,c,** Optical images showing the (**b**) far-view and (**c**) close-view of the QTF with Si tip rigidly mounted.

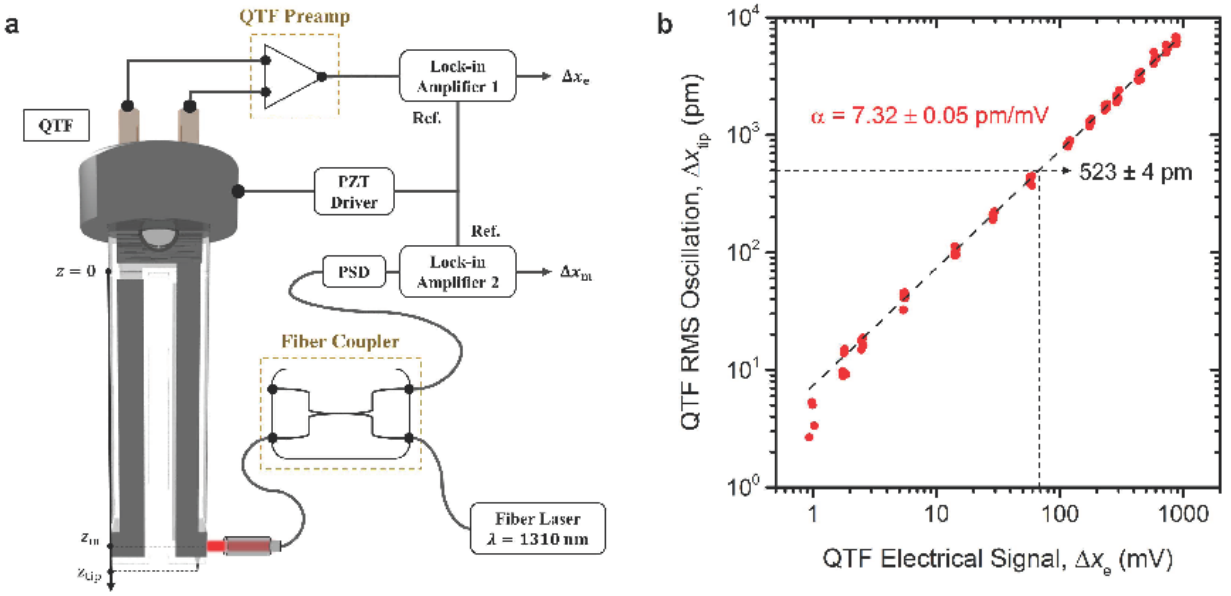

Figure 7: | **QTF oscillation characterization using OFI. a,** Implementation of the OFI system with the QTF for accurate measurement of the QTF oscillation. The QTF geometry was used to linearly related the measured oscillation at z_{m} to the tip motion at z_{tip}. **b,** Relation between the RMS electrical QTF signal and the tip RMS oscillation in picometres. The sensitivity of the QTF signal to lateral deformation in the tines was determined to be 7.32 $\pm$ 0.05 pm/mV. The QTF was nominally operated at an RMS electrical signal of $\sim$70 mV leading to an RMS tip oscillation of $\sim$500 pm.

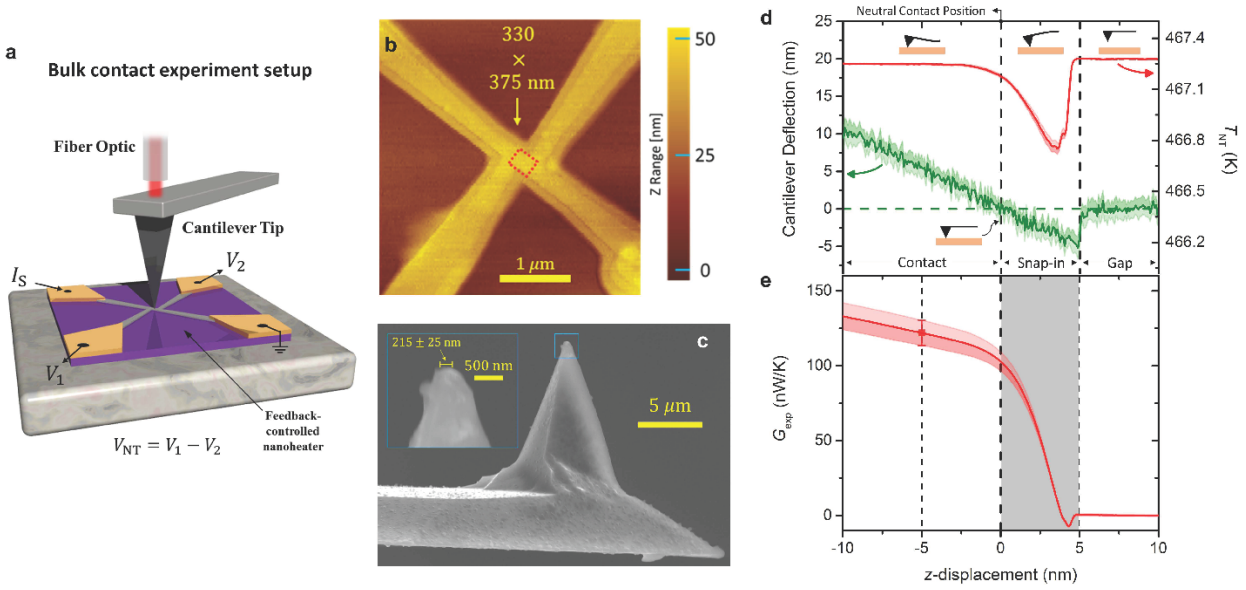

Figure 8: | **Measurement of the bulk-contact thermal conductance (G_{BC}) for the Si-Pt system. a,** Experimental setup, where the Si tip is mounted to the free end of a microcantilever whose deflection is detected by a fiber optic positioned above it. **b,** AFM topographic image of the nanoheater used for the BC experiment with a sensing area of 330 nm $\times$ 375 nm. **c,** SEM image of the cantilever probe tip used for the BC experiment, whose flattened contact diameter is 215$\pm$25 nm. **d,e,** Contact experiment results showing the (**d**) cantilever deflection and feedback-controlled temperature signal, and (**e**) the measured value of G_{exp} as the sample is approached to the tip. Here, G_{BC} for the Si-Pt system at 467 K was measured to be 121.9 $\pm$ 8.4 nW/K extracted from a cantilever deflection of 5 nm (i.e., normal force of $\sim$15 nN). The shaded regions show the 95% confidence interval of 13 measurements, while the solid line represents their average value.

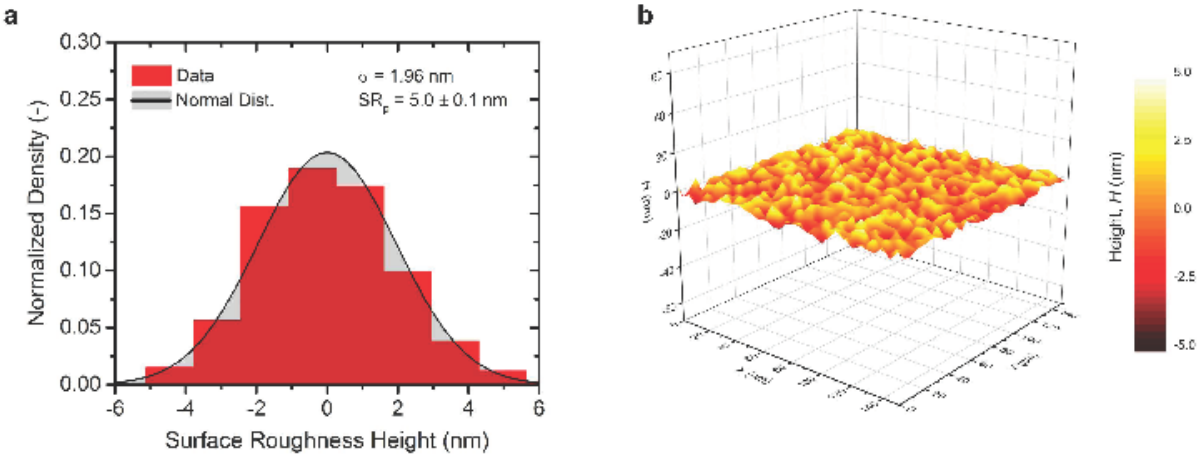

Figure 9: | **Characterization of the nanoheater surface roughness. a,** The AFM topography of the nanoheater sensing region (red rectangle) in Fig. 8c is converted into a histogram which is represented by a Gaussian distribution (black solid line) with $\sigma = 1.96$ nm. The surface roughness peak value within a 98.5% confidence interval was found to be $\mathrm{SR_p} = 5.0 \pm 0.1$ nm. **b,** The Gaussian distribution used to randomly generate 30 surface roughness contours for calculations (one is shown).

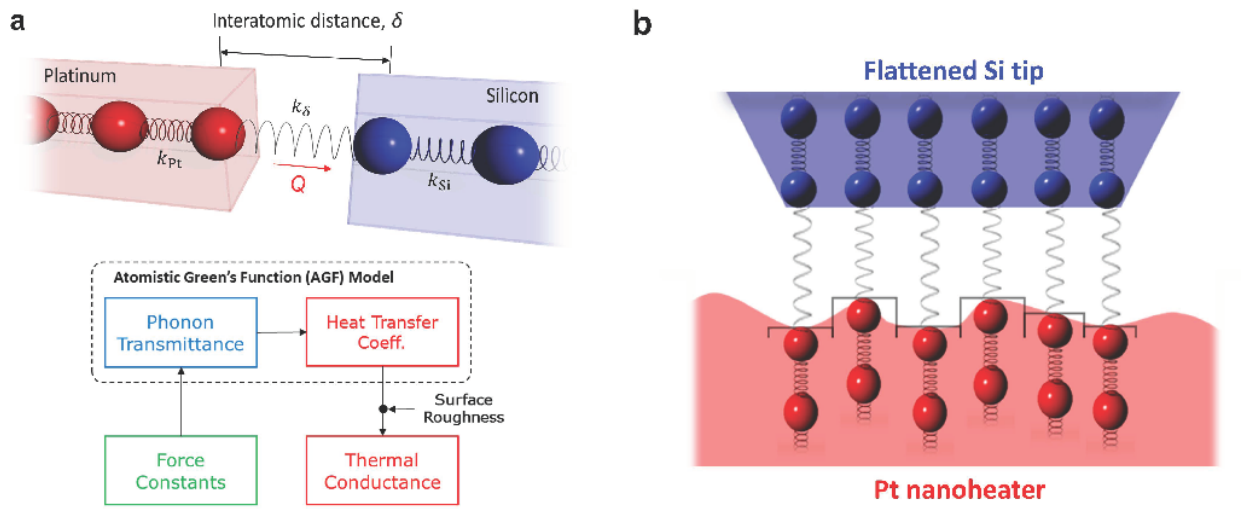

Figure 10: | **Schematics of the AGF method used to rigorously interpret acoustic phonon transport for the Si-Pt system. a,** Simulation domain of the 1D atomic chain system modelled by the AGF method, consisting of a heated Pt bulk region separated by a vacuum gap from a cool Si bulk region. The force constants along the atomic chain (i.e., k_{Pt}, k_δ, and k_{Si}) are used as the input to the AGF. **b,** The generated surface roughness (example shown in Fig. 9b) is used to discretize the Si-Pt surfaces for calculation of the theoretical thermal conductance (G_{theory}). 30 surface roughness contours are used to calculate the 95% confidence interval uncertainty for the theoretical calculations shown in Fig. 4.

Supplementary Information

1. Nanoheater fabrication and calibration

The nanoheaters used in this study were batch fabricated using e-beam lithography for the Pt nanopatterns and photolithography for the Au micro-patterns [50]. The nanoheater is operated using a 4-probe detection scheme as shown in the nanoheater calibration setup (Fig. 11a): while supplying a current ($I_{\rm S}$) along the heater leads, the voltage drop ($V_{\rm NT}$) across the inner electrodes is measured to determine the nanoheater's sensing region resistance ($R_{\rm NT}$). A nanoheater chip is placed on a heater stage equipped with a temperature controller (Cryo-Con, Model 22C) in the HV-SFM vacuum chamber. For nanoheater calibration, the sensing current was set to $I_{\rm S} = 100$ μA to minimize self-heating, while the entire nanoheater chip was bulk-heated in a high vacuum condition (5×10^{-6} Torr) [24]. The calibration results are presented for two devices: nanoheater #1 for the near-contact measurements (Figs. 2c-f), and nanoheater #2 for the bulk-contact measurements (Fig. 4). Figures 11b,d demonstrate the linear proportionality of $R_{\rm NT}$ to the substrate temperature $T_{\rm S}$ (or the sensing area temperature $T_{\rm NT}$), suggesting that $R_{\rm NT}$ can be expressed as $R_{\rm NT} = R_{\rm NT,0}\big[1 + \gamma(T_{\rm NT} - T_{\rm NT,0})\big]$, where γ is the temperature coefficient of resistance (TCR) and the subscript 0 denotes values at room temperature (i.e., 295 K). For nanoheater #1, $R_{\rm NT,0}$ and the TCR are measured to be 5.82 Ω and 1.2×10^{-3} K^{-1}, respectively, while for nanoheater #2 $R_{\rm NT,0} = 4.91$ Ω and $\gamma = 9.6 \times 10^{-4}$ K^{-1}. In order to demonstrate the Joule-heating capability of the nanoheaters, we also measured $R_{\rm NT}$ (or $T_{\rm NT}$) while increasing $I_{\rm S}$ (or power dissipation at the nanoheater sensing region, i.e., $P_{\rm NT} = I_{\rm S} \times V_{\rm NT}$). As shown in Figures 11c,e, the sensing region of both nanoheaters can be Joule-heated up to $\sim$500 K. From the obtained linear correlation between $T_{\rm NT}$ and $P_{\rm NT}$, the effective thermal resistance of the hotspot ($R_{th,\rm NT}$) can be determined by $R_{th,\rm NT} = \Delta T_{\rm NT}/\Delta P_{\rm NT}$, yielding 0.533 ± 0.008 K/μW for nanoheater #1 and 0.485 ± 0.004 K/μW for nanoheater #2, respectively. While the nanoheater TCR calibrations were only performed up to $\sim$350 K due to the limit of the heating stage, the linearity measured between $T_{\rm NT}$ and $P_{\rm NT}$ signifies that the obtained TCRs are valid for higher temperatures.

2. Feedback control of nanoheater sensing region

In the present work, we implement a feedback control scheme into nanoheater operation to accurately measure tip-induced local thermal transport. Based on our previous work [24], the feedback integration gain was set to 20 V/Ω-s to ensure an optimal response of the nanoheaters. Figures 12a,b present $T_{\rm NT}$ and $P_{\rm NT}$ traces of nanoheater #1 when the temperature setpoint was dropped from 481.93 K (or 7.12 Ω) to 479.17 K (7.10 Ω) and returned back to 481.93 K. The nanoheater responds to the stepwise setpoint changes of 2.74 K within a settling time of $\sim$0.5 s and an overshoot temperature of $\sim$0.5 K by changing power dissipation by $\sim$3 μW. As demonstrated in Fig. 2c of the main text, the optimized control scheme allows a stable $T_{\rm NT}$ response at the setpoint within $\pm$50 mK as the tip slowly approaches the nanoheater with a speed of 0.75 nm/s. However, at bulk-contact the tip-induced cooling rate is much faster than the feedback response causing a dramatic drop of $T_{\rm NT}$. This result strongly suggests that the $T_{\rm NT}$ trace can be used to sensitively detect the bulk-contact point, at which the experiment should be stopped to prevent possible damage to the tip and nanoheater.

DC noise characterization of the feedback-controlled nanoheater is important to evaluate the detection limit of the temperature and heat transfer measurement scheme used in the present study. To optimize the response time and signal noise of the nanoheater, an $8^{\rm th}$-order low pass filter with 10 Hz cutoff frequency was implemented, and the feedback gain was set to 20 V/Ω-s as discussed previously. Figs. 12c,d show the $T_{\rm NT}$ and $P_{\rm NT}$ traces with $\pm1\sigma$ statistics for nanoheater #1 at the setpoint of 481.93 K (or 7.12 Ω) and the sampling rate of 500 Hz. The noise-equivalent-temperature (NET) and noise-equivalent-power (NEP) are determined by conducting a time-based statistical analysis of the $T_{\rm NT}$ and $P_{\rm NT}$ traces [51]. For nanoheater #1, the NET and NEP are determined to be 32 mK and 36 nW, respectively. We note that the aggressive low pass filter sufficiently eliminates the power noise at 60 Hz, yielding a three times improvement in the NEP when compared with the previous result [24]. The measured NEP value is in good agreement with the NEP estimated from $R_{th,\rm NT}$ (i.e., NEP = NET/$R_{th,\rm NT} \approx$ 60 nW) [52]. The evaluated NEP confirms that the feedback-controlled nanoheater can precisely measure the tip-induced heat transfer rate in the near-contact regime, which can be as small as $\sim$100 nW for the present study.

3. Estimation of heater lead contribution to $Q_{\rm tip}$

Since the electrical leads outside the nanoheater sensing region are also Joule-heated during feedback-controlled nanoheater operation, its effect onto the tip-induced heat transfer measurement should be carefully characterized. Figures 13a,b show the numerically calculated temperature distribution (COMSOL Multiphysics) of a feedback-controlled nanoheater when a conical silicon tip with 15 nm contact radius is located at the center of the nanoheater

sensing region. Although the feedback controller maintains the average volumetric temperature of the sensing region at T_{NT}, upon the contact of the tip, tip-induced local cooling gives rise to a reversed temperature gradient (i.e., $T_{\mathrm{H}} - T_{\mathrm{NT}}$) around the sensing region (Fig. 13b). Therefore, the heat transfer rate to the tip should be determined by $Q_{\mathrm{tip}} = \Delta P_{\mathrm{NT}} + Q_{\mathrm{Lead}}$, where ΔP_{NT} is the difference of power dissipation in the nanoheater sensing region with ($P_{\mathrm{NT},1}$) and without ($P_{\mathrm{NT},0}$) tip-induced cooling at the same T_{NT}, and Q_{Lead} is the heat transfer rate from the outside leads to the sensing area.

Figures 13c,d illustrate the effective thermal circuits without ($i = 0$) and with ($i = 1$) tip-induced cooling, respectively. When the tip is not present ($i = 0$), $T_{\mathrm{H},0} \approx T_{\mathrm{NT}}$, and the energy balance for the sensing region can be written as:

$$P_{\mathrm{NT},0} \;=\; Q_{\mathrm{loss}}, \tag{13}$$

where Q_{loss} represents the heat loss from the nanoheater sensing region to the ambient at $T_{\infty} = 295$ K. For $i = 1$, the modified temperature profile due to tip cooling provides heat transfer avenues into the sensing region from the two external hotspots (Fig. 13d). Considering these additional heat transfer mechanisms and the symmetry of the nanoheater device, the energy balance for the sensing region can be written as:

$$P_{\mathrm{NT},1} \;+\; Q_{\mathrm{Lead}} \;-\; Q_{\mathrm{tip}} \;-\; Q_{\mathrm{loss}} \;=\; 0. \tag{14}$$

When T_{NT} is constant under temperature feedback control, Q_{loss} is the same for both cases. Therefore, subtracting Eq. (13) from Eq. (14) yields:

$$Q_{\mathrm{tip}} \;=\; \Delta P_{\mathrm{NT}} \;+\; Q_{\mathrm{Lead}}. \tag{15}$$

Eq. (15) illustrates the role of Q_{Lead} to the overall value of Q_{tip}.

Under the assumption that the nanoheater is symmetric and electrical power is applied to the T_{NT} and T_{H} points (Fig. 13d), Q_{Lead} can be approximated as:

$$Q_{\mathrm{Lead}} \;=\; 2\frac{(T_{\mathrm{H},1} \;-\; T_{\mathrm{NT}})}{R_{th,\mathrm{H}}}, \tag{16}$$

where $R_{th,\mathrm{H}}$ is the conductive thermal resistance from the hotspot to the nanoheater sensing region. By considering both thermal circuits, the power supplied to the hotspots in the electrical leads can be written as:

$$P_{\mathrm{H},i} \;= 2\left[\;\frac{(T_{\mathrm{H},i} \;-\; T_{\infty})}{R_{th,\mathrm{L}}} \;+\; \frac{(T_{\mathrm{H},i} \;-\; T_{\mathrm{NT}})}{R_{th,\mathrm{H}}}\right], \tag{17}$$

where $R_{th,\mathrm{L}}$ is the thermal resistance from the heater region to the ambient. In general, the majority of electrical power dissipation in the heater legs conducts through the substrate to ambient (i.e., $R_{th,\mathrm{L}} \ll R_{th,\mathrm{H}}$), such that Eq. (17) can be reduced to $P_{\mathrm{H},i} \approx 2(T_{\mathrm{H},i} - T_{\infty})/R_{th,\mathrm{L}}$. Therefore, it is convenient to define the ratio of heater lead power dissipation with and without tip contact:

$$\frac{P_{\mathrm{H},1}}{P_{\mathrm{H},0}} \;\approx\; \frac{(T_{\mathrm{H},1} \;-\; T_{\infty})}{(T_{\mathrm{H},0} \;-\; T_{\infty})}, \tag{18}$$

and is valid when $R_{th,\mathrm{L}}$ does not significantly vary with temperature. For $i = 0$, the lateral temperature profile is nearly uniform along the sensing region (i.e., $T_{\mathrm{H},0} \approx T_{\mathrm{NT}}$). Therefore, Q_{Lead} can be written as:

$$Q_{\mathrm{Lead}} \;=\; 2\frac{(T_{\mathrm{NT}} \;-\; T_{\infty})}{R_{th,\mathrm{H}}}\left[\frac{P_{\mathrm{H},1}}{P_{\mathrm{H},0}} \;-\; 1\right], \tag{19}$$

by combining Eq. (16) and Eq. (18).

To quantify the effect of Q_{Lead} in Eq. (15), $R_{th,\mathrm{H}}$ must be defined. Under the assumption that heat conduction from the hotspot to the sensing area is dominated by the Pt nanowire, $R_{th,\mathrm{H}}$ can be written as:

$$R_{th,\mathrm{H}} \;=\; \frac{L_{\mathrm{Lead}}}{\kappa A}, \tag{20}$$

where κ is the thermal conductivity of the Pt nanowire, A is its cross-sectional area of the nanoheater sensing region, and L_{Lead} is the effective length of the lead from the outer edge of the inner electrode to the location at T_{H}. Since the Pt nanowire has a sub-100 nm thickness, heat conduction is prone to size effects that reduce κ from its bulk value. To consider these effects in the determination of κ, the Wiedeman-Franz law is used to relate the Pt nanowire's electrical properties, which are readily measured, to its thermal properties. From the Wiedemann-Franz law, the thermal conductivity is expressed as $\kappa = \sigma\mathcal{L}_0 T_{\mathrm{NT}}$, where σ is the electrical conductivity and $\mathcal{L}_0 = 2.44 \times 10^{-}8\ \mathrm{W\Omega/K^2}$ is the Lorenz number. In addition, the electrical conductivity of the Pt nanowire can be written in terms of the sensing

region geometry and electrical resistance, R_{NT}, as $\sigma = L_{\mathrm{NT}}/(R_{\mathrm{NT}}A)$, where L_{NT} is the length of the nanoheater sensing region. Therefore, $R_{th,\mathrm{H}}$ can be rearranged as:

$$R_{th,\mathrm{H}} = \left(\frac{L_{\mathrm{Lead}}}{\mathcal{L}_0 T_{\mathrm{NT}}}\right)\left(\frac{R_{\mathrm{NT}}}{L_{\mathrm{NT}}}\right). \tag{21}$$

Combining Eqs. (19) and (21) yields the final equation for Q_{tip} as:

$$Q_{\mathrm{tip}} = \Delta P_{\mathrm{NT}} + \frac{2\mathcal{L}_0 T_{\mathrm{NT}} L_{\mathrm{NT}}(T_{\mathrm{NT}} - T_\infty)}{L_{\mathrm{Lead}} R_{\mathrm{NT}}}\left[\frac{P_{\mathrm{H},1}}{P_{\mathrm{H},0}} - 1\right]. \tag{22}$$

In Eq. (22), all variables except L_{Lead} are readily determined from the nanoheater geometry and tip-approaching experiments. L_{Lead} is determined by imaging the electrical resistance of the entire nanoheater while an Si cantilever tip raster scans the heated nanoheater without feedback control in contact mode [50]. Figure 13e shows the tip-scanned heater resistance image when the nanoheater is heated at $T_{\mathrm{NT}} = 467.25$ K, demonstrating that the heater resistance becomes the lowest when the tip is positioned at the local hotspot of the lead due to the maximum tip-induced cooling. In this image, the locations of the heater lead hotspots are determined to be approximately 520 nm away from the outer edge of the inner electrodes (i.e., $L_{\mathrm{Lead}} \approx 520$ nm).

4. Estimation of temperature rise in the tip apex

To define G_{exp} in both the near-contact and bulk-contact experiments, the temperature gradient across the nanogap/interface was defined as $\Delta T = T_{\mathrm{NT}} - T_{\mathrm{tip}}$. While T_{NT} is readily determined using the feedback-controlled nanoheaters, the direct measurement of T_{tip} requires a functionalized thermocouple tip [53]. Since it is challenging to integrate such devices with the QTF, we have made use of COMSOL Multiphysics simultations to predict the temperature rise in the Si tip apex due to the heat transfer rate experienced during bulk-contact ($Q_{\mathrm{tip,BC}} = 10.2$ μW at $d = 0$ in Fig. 2e). The geometric profile of the tip used in the near-contact measurements is obtained using SEM (Fig. 14a). This profile is traced and revolved about its central axis to give a conical representation of the tip for simulation (Fig. 14b,c). The backside of the tip is assumed at room temperature ($T_\infty = 295$ K), while the side walls are insulated. Fig. 14c shows the simulated temperature distribution of the tip, where the tip apex temperature is elevated by $\Delta T_{\mathrm{Si}} = 0.6$ K above T_∞. The tip thermal resistance can be calculated by $R_{th,\mathrm{tip}} = \Delta T_{\mathrm{Si}}/Q_{\mathrm{tip,BC}} = 0.054$ K/μW, which is more than two orders of magnitude smaller than the BC thermal resistance of $R_{th,\mathrm{BC}} \approx 17$ K/μW measured in the experiments. Due to the significantly small $R_{th,\mathrm{tip}}$ compared to $R_{th,\mathrm{BC}}$, the temperature rise in the tip apex during the experiments is ignored, such that $T_{\mathrm{tip}} \approx 295$ K.

5. Calculation of force constants for the AGF method

Both short-range and long-range interactions are considered for modeling force-induced acoustic phonon heat transport across vacuum gaps. In this work, short-range interactions are modelled via the Lennard-Jones (L-J) potential. For the long-range interactions, both electrostatic and electric field-driven forces are taken into account. It should be noted that the electrostatic interaction is typically caused by the ion binding properties of a system [22]. The existence of ion binding can be estimated through the ionic character of a system as follows [54]:

$$\text{Ionic character } [\%] = \left[1 - e^{(\Delta\chi/2)^2}\right] \times 100, \tag{23}$$

where the dimensionless quantity $\Delta\chi$ is the electronegativity between two elements. The electronegativity of Pt and Si atoms are $\chi_{\mathrm{Pt}} = 2.2$ and $\chi_{\mathrm{Si}} = 1.8$ [54], respectively, leading to an ionic character of 3.92 % for the Pt-Si system. Therefore, electrostatic force due to ion binding is negligible. Yet, the bias voltage of 0.8 V at the Pt nanoheater sensing region induces surface charges resulting in electrostatic forces, modeled here as Coulomb and capacitor forces [55]. For the electric field-driven interaction, Casimir force is considered. The total force driving acoustic phonon transport across vacuum gaps is therefore the sum of L-J, Casimir, Coulomb and capacitor forces:

$$F_{\mathrm{total}} = F_{\mathrm{L-J}} + F_{\mathrm{Casimir}} + F_{\mathrm{Coulomb}} + F_{\mathrm{capacitor}}, \tag{24}$$

In the AGF method, force constants (i.e., first derivative of force) are required for calculating phonon transmission. The determination of $F_{\mathrm{L-J}}$, F_{Casimir}, F_{Coulomb} and $F_{\mathrm{capacitor}}$ is provided in the following subsections.

5.1 Lennard-Jones (L-J) force model

The L-J potential is given by [56]:

$$U_{\mathrm{L-J}} = 4\varepsilon\left[\left(\frac{\sigma}{\delta}\right)^{12} - \left(\frac{\sigma}{\delta}\right)^{6}\right] \tag{25}$$

where $\varepsilon = 4.80\times10^{-20}$ J and $\sigma = 1.84\times10^{-10}$ m [57]. The derivative of Eq.(25) with respect to the interatomic distance, δ, provides the L-J force:

$$F_{\mathrm{L-J}} \;=\; -24\left(\frac{\varepsilon}{\delta}\right)\left[2\left(\frac{\sigma}{\delta}\right)^{12}-\left(\frac{\sigma}{\delta}\right)^{6}\right], \tag{26}$$

The force constant in N/m needed for AGF calculations is obtained by taking the absolute value of the derivative of Eq. (26) with respect to δ [21]:

$$k_{\mathrm{L-J}} \;=\; \left|24\varepsilon\left[26\left(\frac{\sigma^{12}}{\delta^{14}}\right)-7\left(\frac{\sigma^{6}}{\delta^{8}}\right)\right]\right| \tag{27}$$

5.2 Casimir force model

The Casimir force is calculated via the Lifshitz model as follows [58]:

$$F_{\mathrm{Casimir}} \;=\; A_{\mathrm{Si-Pt}}\frac{\hbar}{16\pi^2\delta^3}\int_{\xi=0}^{\infty}\left\{\int_{x=0}^{\infty}\frac{x^2}{\left[\frac{\varepsilon_{\mathrm{Si}}(i\xi)+1}{\varepsilon_{\mathrm{Si}}(i\xi)-1}\right]\left[\frac{\varepsilon_{\mathrm{Pt}}(i\xi)+1}{\varepsilon_{\mathrm{Pt}}(i\xi)-1}\right]e^{x}-1}dx\right\}d\xi \tag{28}$$

where $\varepsilon_{\mathrm{Si}}$ and $\varepsilon_{\mathrm{Pt}}$ are the dielectric functions of Si and Pt. The upper limit of the integration over ξ is taken as $10k_{\mathrm{b}}T/\hbar$ [21], where T is treated as the average temperature of Si and Pt (385 K). The integration over x in Eq. (28) is performed using the double exponential formula [59], while a trapezoidal numerical scheme is employed for the integration with respect to ξ. The Casimir force constant in N/m is given by [21]:

$$k_{\mathrm{Casimir}} \;=\; \left|-A_{\mathrm{Si-Pt}}\frac{3\hbar}{16\pi^2\delta^4}\int_{\xi=0}^{\infty}\left\{\int_{x=0}^{\infty}\frac{x^2}{\left[\frac{\varepsilon_{\mathrm{Si}}(i\xi)+1}{\varepsilon_{\mathrm{Si}}(i\xi)-1}\right]\left[\frac{\varepsilon_{\mathrm{Pt}}(i\xi)+1}{\varepsilon_{\mathrm{Pt}}(i\xi)-1}\right]e^{x}-1}dx\right\}d\xi\right| \tag{29}$$

5.3 Coulomb force model

The Coulomb force is mediated by surface charges. The Pt nanoheater sensing region has negative surface charges due to the applied bias voltage V_{bias} of 0.8 V. By assuming the Si tip as a floating ground, positive image charges are induced at the tip apex. Surface charges of opposite signs are the source of Coulomb and capacitor forces. The Coulomb force due to surface charges is given by [60]:

$$F_{\mathrm{Coulomb}} \;=\; \frac{Q_{\mathrm{s}}Q_{\mathrm{t}}}{4\pi\varepsilon_0\delta^2}, \tag{30}$$

where ε_0 is the permittivity of free space, Q_{s} is the surface charge, and Q_{t} is the tip charge defined as $Q_{\mathrm{t}} = -(Q_{\mathrm{s}}+Q_{\mathrm{e}})$. Q_{e} is the induced capacitive charge [61] given by $Q_{\mathrm{e}} = CV_{\mathrm{bias}}$, where C $(= \varepsilon_0 A_{\mathrm{tip}}/\delta)$ is the parallel plate capacitance. In this work, Q_{s} is determined from our experiment (See Section 5.7). Since Eq. (30) describes force on the entire tip surface, area conversion is required for obtaining the force constant between Si and Pt atoms. By using the Si-Pt average atomic area, $A_{\mathrm{Si-Pt}}$, the Coulomb force constant can be written as follows [21]:

$$k_{\mathrm{Coulomb}} \;=\; \left|\frac{\partial F_{\mathrm{Coulomb}}}{\partial\delta}\cdot\frac{A_{\mathrm{Si-Pt}}}{A_{\mathrm{tip}}}\right| = \left|\frac{Q_{\mathrm{s}}}{4\pi\varepsilon_0}\left(\frac{2Q_s}{\delta^3}+\frac{3\varepsilon_0 V_{\mathrm{bias}}A_{\mathrm{tip}}}{\delta^4}\right)\cdot\frac{A_{\mathrm{Si-Pt}}}{A_{\mathrm{tip}}}\right| \tag{31}$$

5.4 Capacitor force model

The capacitor force of a planar surface is given by [62]:

$$F_{\mathrm{capacitor}} \;=\; \frac{\varepsilon_0 V^2}{2}\frac{A_{\mathrm{tip}}}{\delta^2} \tag{32}$$

where $V = V_{\mathrm{bias}} - \Delta\Phi$ [63]. $\Delta\Phi$ is the difference of the Si and Pt workfunctions [63]. The work functions for Pt (Φ_{Pt}) and Si (Φ_{Si}) are set to 5.80 eV and 4.70 eV, respectively, which are within ranges reported in the literature [64–66]. Since Eq. (32) describes force on the entire tip surface, the force constant due capacitor force between Si and Pt atoms can be written as [21]:

$$k_{\mathrm{capacitor}} \;=\; \left|\frac{\partial F_{\mathrm{capacitor}}}{\partial\delta}\cdot\frac{A_{\mathrm{Si-Pt}}}{A_{\mathrm{tip}}}\right| = \left|-\frac{\varepsilon_0 V^2 A_{\mathrm{tip}}}{\delta^3}\cdot\frac{A_{\mathrm{Si-Pt}}}{A_{\mathrm{tip}}}\right| \tag{33}$$

It should be noted that the heat transfer coefficient by the capacitor force is negligibly small compared to that of the Coulomb force. For example, at $\delta = 5$ nm the capacitive and Coulomb heat transfer coefficients are found to be 10^1 and 10^4 $\mathrm{W/m^2K}$, respectively. Therefore, the heat transfer coefficient due to the capacitor force and its contribution to the thermal conductance are not shown in Figs. 3a and 4c.

5.5 Effect of charge neutralization on the Coulomb and capacitor forces

At some small vacuum distance before contact, the Coulomb and capacitor forces begin to vanish due to charge neutralization [67]. The reduction of Q_{s} with respect to the gap distance between a tip and substrate has been numerically predicted in the literature [68, 69]. An experimental study has also demonstrated a vanishing capacitance between a tip and substrate with the reduction of the gap distance [70]. As such, Q_{s} should ideally be treated as a function of δ [69]. However, since it is inherently challenging to develop a mathematical model of gap-dependent surface charge, the present work treats Q_{s} as a fixed value that vanishes at a cutoff gap distance [71]. The cutoff distance is determined at the onset of electron tunneling across the gap, which is set to an interatomic distance $\delta \approx 12\,\text{Å}$ [72, 73]. This interatomic distance cutoff corresponds to a gap distance of $\bar{\delta} = 9.1\,\text{Å}$, where $\bar{\delta} = \delta - r_{\mathrm{Si}} - r_{\mathrm{Pt}}$. For example, the electron tunneling distance between gold STM probe and gold substrate is estimated to occur at a gap distance of 10 Å at room temperature [72]. By applying a cutoff distance, both the Coulomb and capacitor forces become zero below the cutoff distance. The reduction of electrostatic force due to partial neutralization of surface charges has been experimentally observed [74].

5.6 Interatomic force constants of Si and Pt

The interatomic force constants of Pt atoms (k_{Pt}) in the left region and Si atoms (k_{Si}) in the right region are required as the inputs for AGF calculations. $k_{\mathrm{Pt}} = 6.31\ \mathrm{N/m}$ is obtained from the second derivative of the L-J potential using $\varepsilon = 1.09{\times}10^{-19}$ J and $\sigma = 2.54{\times}10^{-10}$ m for Pt-Pt [57]. $k_{\mathrm{Si-Si}} = 6.16\ \mathrm{N/m}$ is taken from Ref. [21].

5.7 Determination of the Si-Pt surface charge density

As discussed previously, the surface charge density is required to accurately calculate the Coulomb force contribution to the thermal transport between charged surfaces separated by single-digit nanometre vacuum gap distances. Several experimental results have attempted to measure its value for various materials [61, 75–77]. For example, given a metal tip and substrate, the surface charge density was measured to be $1.40{\times}10^{-4}\ \mathrm{C/m^2}$ [75] and was similarly found to be $2.50{\times}10^{-4}\ \mathrm{C/m^2}$ for a metal tip and resin substrate [61]. For a resin tip and resin substrate, the surface charge density can be as high as $1.40{\times}10^{-2}\ \mathrm{C/m^2}$ [76], while for semiconductors the order of the surface charge density is given from $10^{-3}{\sim}\,10^{-2}\ \mathrm{C/m^2}$ [77]. From these experimental results a reasonable range for the surface charge density is $10^{-4}\ \sim 10^{-2}\ \mathrm{C/m^2}$ [61, 75–77]. Moreover, it is very challenging to numerically predict the surface charge density as it inevitably depends on the material properties, bias voltage, temperature, and gap distance. To constrain these parameters for our experimental condition, we extract the surface charge density from the lateral force measurement using the gap-dependent Δf signal of the QTF (Fig. 15). It should be noted that Δf is independently measured from the nanoheater signals and inherently contains the dominant effects of the material properties, bias voltage, temperature, and gap distance. Thus interpretation of the surface charge density from the measured lateral force is the most consistent method to constrain the unknown parameter dependencies.

The Coulomb force is given by Eq. (30), where $Q_{\mathrm{s}} = \sigma_{\mathrm{s}} A_{\mathrm{tip}}$ and σ_{s} is the surface charge density. In the near-contact regime (i.e., sub-2-nm gaps before asperity contact) attractive Coulomb forces are expected to be dominant (Fig. 4). Therefore, we used the lateral force measurement of 0.22 nN-rms at d = 6 nm (Fig. 15) to calculate the nominal surface charge density based on the flat plate approximation of the Coulomb force equation. To do this, we assume μ = 0.001 as the near-contact friction coefficient enabling the conversion of lateral force to normal force. We believe this value is within the acceptable range for the Si-Pt system with a nanoscale gap because experimental measurements of the contact μ value ranges from ∼0.1 to ∼0.01 depending on the contacting area [78]. Furthermore, molecular dynamics simulations for lubricated atomically flat surfaces in contact predicted $\mu \sim 0.001$ [79]. Using $\mu = 0.001$, σ_{s} was estimated to be $8 \times 10^{-4}\ \mathrm{C/m^2}$. We established a confidence interval for the near-contact μ ranging from 0.002 to 0.0007 , which corresponds to a surface charge density range of 6×10^{-4} to $1 \times 10^{-3}\ \mathrm{C/m^2}$. These values of the surface charge density in conjunction with the surface roughness distributions were used to determine the theoretical uncertainties shown in Fig. 4.

6. Verification of 1D AGF method

The force-induced acoustic phonon heat transfer coefficient calculated via the AGF method is compared against various theoretical and experimental results for verification purpose. Figure 16 and Table 1 show comparison results for an Si-Si system. The black dots in Figure 16 show the heat transfer coefficient calculated by three-dimensional (3D) lattice dynamics (LD) for the Si-Si system at 300 K using the Stillinger-Weber potential [20]. Results from the one-dimensional (1D) AGF (this work) for the same Si-Si system at 300 K using the Stillinger-Weber potential are plotted using a red solid line. Results from the 1D AGF model compares well with 3D LD, such that a 1D approximation of acoustic

phonon transport should be sufficient to describe the near-contact heat transfer for the Si-Pt system. In addition, Table 1 presents the Si-Si interfacial heat transfer coefficient obtained via different theoretical methods including the 1D AGF (this work), 3D LD [20], 3D AGF, and an experiment [80–82]. The 1D AGF is good agreement with each theoretical result from the literature illustrating that a 1D approximation is sufficient when considering interfacial thermal transport. It should be noted the lower and upper limits of the experimental result come from the different terminating states of the Si atoms: (lower) hydrogen-terminated and (upper) between the hydrogen-terminated and oxide-terminated interfaces [82]. We believe that the slight discrepancy between our calculations and experimental results in the near-contact regime in Fig. 4a may be due to 3D effects that arise across a vacuum gap.

7. Electronic heat transfer coefficient

Electrons may also contribute to heat transfer via tunneling and thermionic emission. However, only electron tunneling is considered in the present study as thermionic emission requires high temperatures (e.g., $\sim 1360 - 1750$ K for Pt and $\sim 827 - 1077$ K for Si [65, 83]). For biased Pt (L) and Si (R), the heat flux due to electron tunneling can be written as [84]:

$$q_{\mathrm{el}} \;=\; \int dE_z \left[\left(E_z + k_{\mathrm{b}} T_{\mathrm{L}}\right) N_L \left(E_z - eV_{\mathrm{bias}}, T_{\mathrm{L}}\right) - \left(E_z + k_{\mathrm{b}} T_{\mathrm{R}}\right) N_R \left(E_z, T_{\mathrm{R}}\right) \right] \mathcal{T}_{\mathrm{el}} \left(E_z\right) \tag{34}$$

where $e = 1.602{\times}10^{-19}$ C is the charge of a single electron, $V_{\mathrm{bias}} = 0.8$ V is the voltage bias at the Pt nanoheater sensing region, and E_z is the electron energy perpendicular to an interface. Eq. (34) is integrated from $E_G/2$ to W_{max}, where E_G is the bandgap of Si and W_{max} is the maximum potential energy barrier, based on the assumption that the tip is made of intrinsic Si to have its Fermi level in the middle of the bandgap. Therefore, only electrons in Pt above the conduction band of Si are allowed to tunnel through to Si [85]. $N_i(E_z, T_i)$ denotes the number of electrons at energy level E_z per unit area and unit time, and can be calculated by:

$$N_i \left(E_z, T_i\right) \;=\; \frac{m_e k_{\mathrm{b}} T_i}{2\pi^2 \hbar^3} \ln \left[1 + \exp\left(- \frac{E_z - E_{F,i}}{k_{\mathrm{b}} T_i} \right) \right] \tag{35}$$

where $m_{\mathrm{e}} = 9.109 \times 10^{-31}$ kg is the electron mass, and E_F is the Fermi energy level. The electron transmission function, $\mathcal{T}_{\mathrm{el}}\left(E_z\right)$, is calculated based on the Wentzel-Kramers-Brillouin (WKB) approximation:

$$\mathcal{T}_{\mathrm{el}} \left(E_z\right) \;=\; \exp\left[- \frac{\sqrt{8 m_e}}{\hbar} \int_{z_1}^{z_2} dz \sqrt{W\left(z\right) - E_z} \right] \tag{36}$$

where z_1 and z_2 are the roots of $W(z) - E_z = 0$, representing the effective gap distance of the electron tunneling at E_z. In the ideal case, the potential energy profile across the vacuum gap can be expressed as:

$$W(z) = \Phi_{\mathrm{Pt}} + eV_{\mathrm{bias}} - \left(\Phi_{\mathrm{Pt}} + eV_{\mathrm{bias}} - \Phi_{\mathrm{Si}}\right) \left(\frac{z}{d}\right) \tag{37}$$

where $\Phi_{\mathrm{Pt}} = 5.80\,\mathrm{eV}$ and $\Phi_{\mathrm{Si}} = 4.70\,\mathrm{eV}$ are the work functions of Pt and Si, respectively. The maximum potential energy barrier can then be written as $W_{\mathrm{max}} = \Phi_{\mathrm{Pt}} + eV_{\mathrm{bias}}$ at $z = 0$. Although electrostatic interactions between tunneling electrons and image charges within the nanoheater and the tip may lower the potential barrier below the ideal profile [86], this image charge effect is not considered in the present study for simplicity. In addition, the space charge effect is asuumed to be fully suppressed for single-digit nanometre vacuum gaps [87].

The electronic heat transfer coefficient, h_{el}, is calculated by $h_{\mathrm{el}} = q_{\mathrm{el}}/\Delta T$. For a vacuum gap distance of $\bar{\delta} = 1$ nm, h_{el} is calculated to be $2.5\ \mathrm{W/m^2K}$, which is orders of magnitude smaller than the force-induced acoustic phonon heat transfer coefficients (Fig. 3a in the Main text). Since h_{el} is negligible, the overall heat transfer coefficient is calculated by $h = h_{\mathrm{rad}} + h_{\mathrm{ph}}$, where h_{rad} and h_{ph} are the heat transfer coefficients due to near-field thermal radiation and force-induced acoustic phonon transport, respectively.

Supplementary References

[50] Hamian, S., Yun, J., Park, I. & Park, K. Quantitative probing of tip-induced local cooling with a resistive nanoheater/thermometer. *Applied Physics Letters* **109**, 253114 (2016).

[51] Bentley, J. P. *Principles of Measurement Systems* (Longman Group Limited, Essex, England, 1995), 3rd edn.

[52] Sadat, S., Meyhofer, E. & Reddy, P. High resolution resistive thermometry for micro/nanoscale measurements. *Review of Scientific Instruments* **83**, 084902 (2012).

[53] Kim, K., Jeong, W., Lee, W. & Reddy, P. Ultra-high vacuum scanning thermal microscopy for nanometer resolution quantitative thermometry. *ACS Nano* **6**, 4248–4257 (2012).

[54] Pauling, L. *The Nature of the Chemical Bond* (Cornell University Press, Ithaca, NY, 1960).

[55] Shockley, W. & Pearson, G. L. Modulation of conductance of thin films of semi-conductors by surface charges. *Physical Review* **74**, 232–233 (1948).

[56] J.E. Jones. On the Determination o f Molecular Fields.-II. From the Equation o f State o f a Gas. *Proceedings of the Royal Society A* **106**, 463 (1924).

[57] Webb, E. B. & Garofalini, S. H. Molecular dynamics simulation of elevated temperature interfacial behavior between silica glass and a model crystal. *Journal of Chemical Physics* **105**, 792–801 (1996).

[58] Lifshitz, E. The theory of molecular attractive forces between solids. *Journal of Experimental and Theoretical Physics* **2**, 73–83 (1956).

[59] Takahasi, H. & Mori, M. Double exponential formulas for numerical integration. *Publications of the Research Institute for Mathematical Sciences* **9**, 721–741 (1974).

[60] Terris, B. D., Stern, J. E., Rugar, D. & Mamin, H. J. Contact electrification using force microscopy the principles of force microscopy. *Physical Review Letters* **63**, 2669–2672 (1989).

[61] El Khoury, D., Arinero, R., Laurentie, J. C. & Castellon, J. Nanoscale surface charge detection in epoxy resin materials using electrostatic force spectroscopy. *AIP Advances* **6**, 035318 (2016).

[62] Belaidi, S., Girard, P. & Leveque, G. Electrostatic forces acting on the tip in atomic force microscopy: Modelization and comparison with analytic expressions. *Journal of Applied Physics* **81**, 1023–1030 (1997).

[63] Burke, S. A. *et al.* Determination of the local contact potential difference of PTCDA on NaCl: Acomparison of techniques. *Nanotechnology* **20**, 264012 (2009).

[64] Kaack, M. & Fick, D. Determination of the work functions of Pt (lll) and Ir (lll) beyond 1100 K surface temperature. *Surface Science* **342**, 111–118 (1995).

[65] Esaki, L. Electrical Resistivity and Thermionic Emission of Silicon. *Journal of the Physical Society of Japan* **8**, 347–349 (1953).

[66] Dillon, J. A. & Farnsworth, H. E. Work function and sorption properties of silicon crystals. *Journal of Applied Physics* **29**, 1195–1202 (1958).

[67] Srisonphan, S., Kim, M. & Kim, H. K. Space charge neutralization by electron-transparent suspended graphene. *Scientific Reports* **4**, 3764 (2014).

[68] Hong, J., Noh, K. & il Park, S. Surface charge density and evolution of domain structure in triglycine sulfate determined by electrostatic-force microscopy. *Physical Review B - Condensed Matter and Materials Physics* **58**, 5078–5084 (1998).

[69] Behrens, S. H. & Grier, D. G. The charge of glass and silica surfaces. *Journal of Chemical Physics* **115**, 6716 (2001).

[70] Yoo, M. J., Hoskins, B. F., Robson, R. & Chem, J. A. Imaging Individual Charges Scanning Single-Electron Transistor Microscopy : Imaging Individual Charges. *Science* **579**, 579–582 (2007).

[71] Butt, H.-J. Electrostatic interaction in atomic force microscopy. *Biophysical Journal* **60**, 777–785 (1991).

[72] Anselmetti, D. *et al.* Single-electron tunnelling at room temperature with adjustable double-barrier junctions. *Europhysics Letters* **25**, 297–302 (1994).

[73] McCarty, L. S. & Whitesides, G. M. Electrostatic charging due to separation of ions at interfaces: Contact electrification of ionic electrets. *Angewandte Chemie - International Edition* **47**, 2188–2207 (2008).

[74] Horn, R. G., Smith, D. T. & Grabbe, A. Contact electrification induced by monolayer modification of a surface and relation to acid-base interactions. *Nature* **366**, 442–443 (1993).

[75] Johann, F. & Soergel, E. Quantitative measurement of the surface charge density. *Applied Physics Letters* **95**, 232906 (2009).

[76] Klausen, L. H., Fuhs, T. & Dong, M. Mapping surface charge density of lipid bilayers by quantitative surface conductivity microscopy. *Nature Communications* **7**, 12447 (2016).

[77] Yang, Y., Mayer, K. M. & Hafner, J. H. Quantitative membrane electrostatics with the atomic force microscope. *Biophysical Journal* **92**, 1966–1974 (2007).

[78] Bhushan, B. & Kwak, K. J. Platinum-coated probes sliding at up to 100 mm/s against coated silicon wafers for AFM probe-based recording technology. *Nanotechnology* **18**, 345504 (2007).

[79] Gao, J. *et al.* Frictional Forces and Amontons' Law: From the Molecular to the Macroscopic Scale. *The Journal of Physical Chemistry B* **108**, 3410–3425 (2004).

[80] Zhang, W., Fisher, T. S. & Mingo, N. Simulation of Interfacial Phonon Transport in SiGe Heterostructures Using an Atomistic Green's Function Method. *Journal of Heat Transfer* **129**, 483–491 (2007).

[81] Landry, E. S. & McGaughey, A. J. Thermal boundary resistance predictions from molecular dynamics simulations and theoretical calculations. *Physical Review B* **80**, 165304 (2009).

[82] Schroeder, D. P. *et al.* Thermal resistance of transferred-silicon-nanomembrane interfaces. *Physical Review Letters* **115**, 256101 (2015).

[83] Dubridge, L. A. The thermionic emission from clean platinum. *Physical Review* **32**, 961–966 (1928).

[84] Hishinuma, Y., Geballe, T. H., Moyzhes, B. Y. & Kenny, T. W. Refrigeration by combined tunneling and thermionic emission in vacuum: Use of nanometer scale design. *Applied Physics Letters* **78**, 2572–2574 (2001).

[85] Chang, L. L., Stiles, P. J. & Esaki, L. Electron tunneling between a metal and a semiconductor: Characteristics of Al-Al2O3-SnTe and -GeTe junctions. *Journal of Applied Physics* **38**, 4440–4445 (1967).

[86] Baeva, M. Application of the transferred matrix method to a unified evaluation of the cathodic electron emission. *AIP Advances* **8**, 085322 (2018).

[87] Wang, Y. *et al.* Effects of nanoscale vacuum gap on photon-enhanced thermionic emission devices. *Journal of Applied Physics* **119**, 045106 (2016).

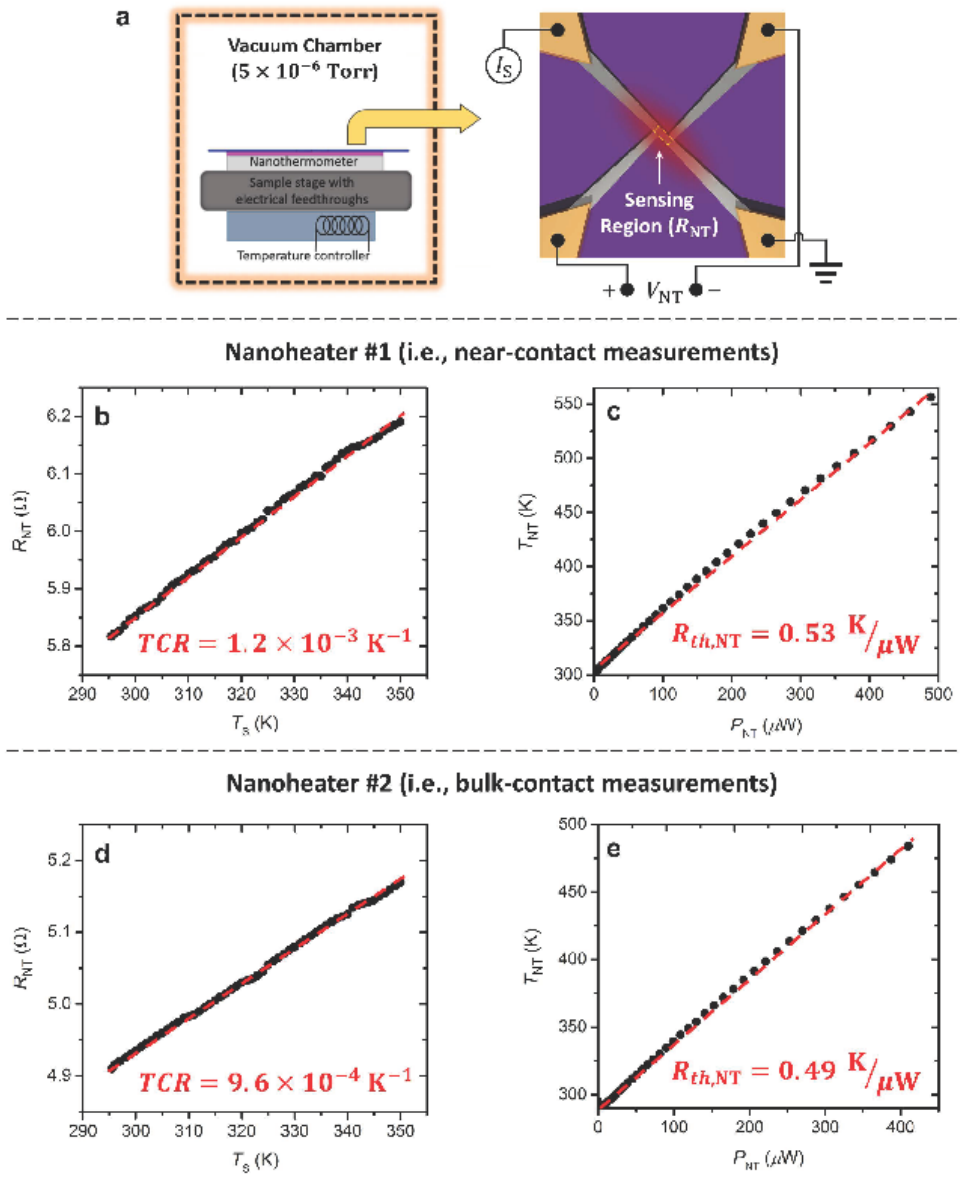

Figure 11: | **Calibration of the main nanoheater devices. a,** Schematic of the calibration setup for the nanoheaters. **b,** Temperature coefficient of resistance (TCR) calibration for nanoheater #1 showing a linear relationship between the nanoheater sensing region resistance (R_{NT}) and the substrate temperature (T_{S}). Based on the linear trend, the TCR of nanoheater #1 is 1.2×10^{-3} K^{-1}. **c,** Calibration of the sensing region thermal resistance for nanoheater #1 ($R_{\mathrm{th,NT}}$) by relating its temperature with its power dissipation. For nanoheater #1, $R_{\mathrm{th,NT}}$ was found to be 0.53 ± 0.008 K/μW. **d,e,** Same as (**b,c**) but for nanoheater #2 where the TCR and $\mathrm{R}_{th,\mathrm{NT}}$ were determined to be 9.6×10^{-4} K^{-1} and 0.485 ± 0.004 K/μW, respectively.

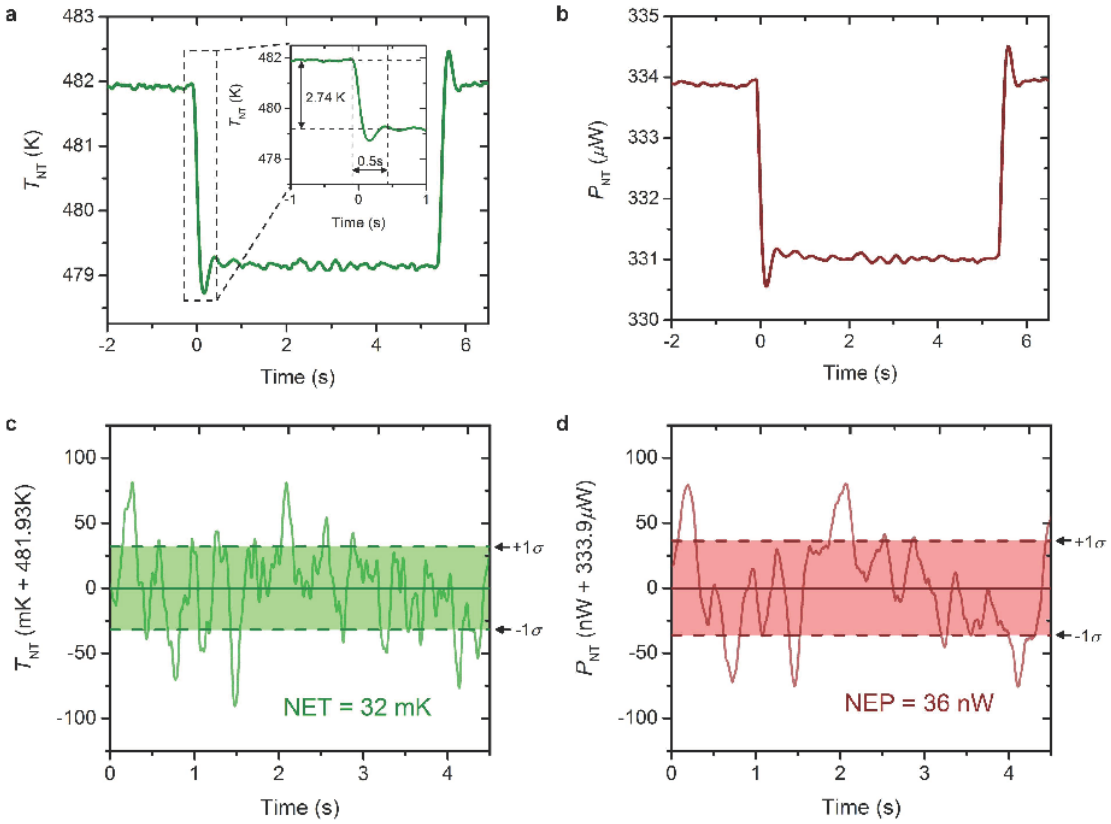

Figure 12: | **Characterization of the feedback-controlled nanoheater operation and its DC noise. a,** Transient response of T_{NT} during temperature feedback control ($G = 20$ V/Ω-s) when the temperature setpoint is step-wise changed between 481.93 K and 479.19 K. (inset) shows the applied temperature change of 2.74 K for the cooling case, which requires 0.5 s to fully settle. **b,** The corresponding P_{NT} measurement required to stabilize the temperature at the setpoint. **c,d,** Statistical analysis implemented to determine the (**c**) noise-equivalent-temperature (NET) and (**d**) noise-equivalent-power (NEP) resolutions for DC operation of the nanoheater under temperature feedback control. The $\pm 1\sigma$ NET and NEP were determined to be 32 mK and 36 nW, respectively.

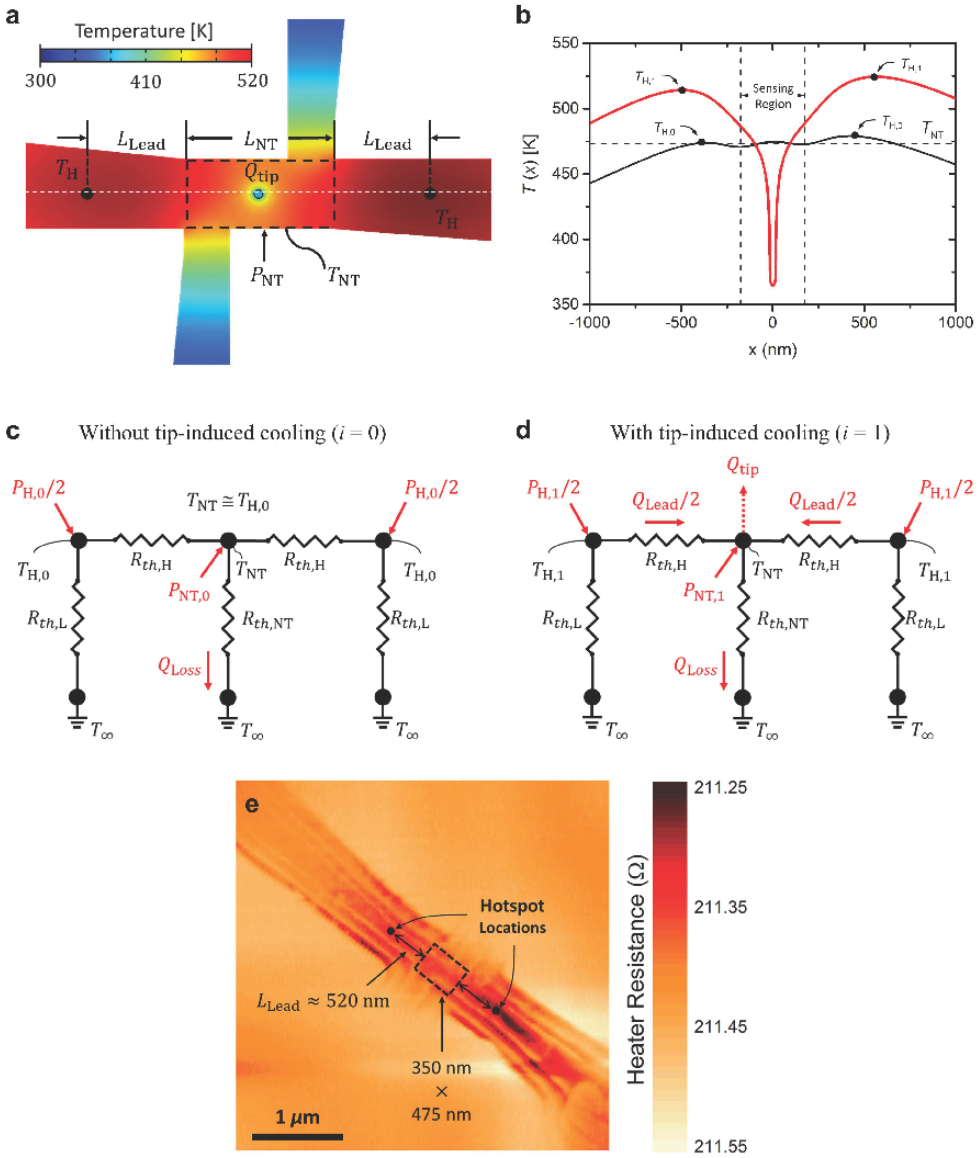

Figure 13: | **Analysis of heater lead contribution. a,** Simulated temperature distribution of the nanoheater showing the characteristic temperatures and definitions used in the network analysis. **b,** Surface line profile temperature extracted from the white dashed line in (**a**). It should be noted that in the simulations, T_{NT} is defined as the volumetric average temperature of the sensing region and is set to 467 K. **c,d,** Thermal circuit analysis of the nanoheater without ($i = 0$) and with ($i = 1$) tip contact used to derive Eq. (22). **e,** Experimental heater resistance image acquired as a cool Si tip is raster scanned over the hot nanoheater without the use of temperature feedback control. Tip-induced cooling causes the local resistance (or temperature) of the heater to drop. Thus, darker regions in the image are attributed to hotspots with more tip-induced cooling.

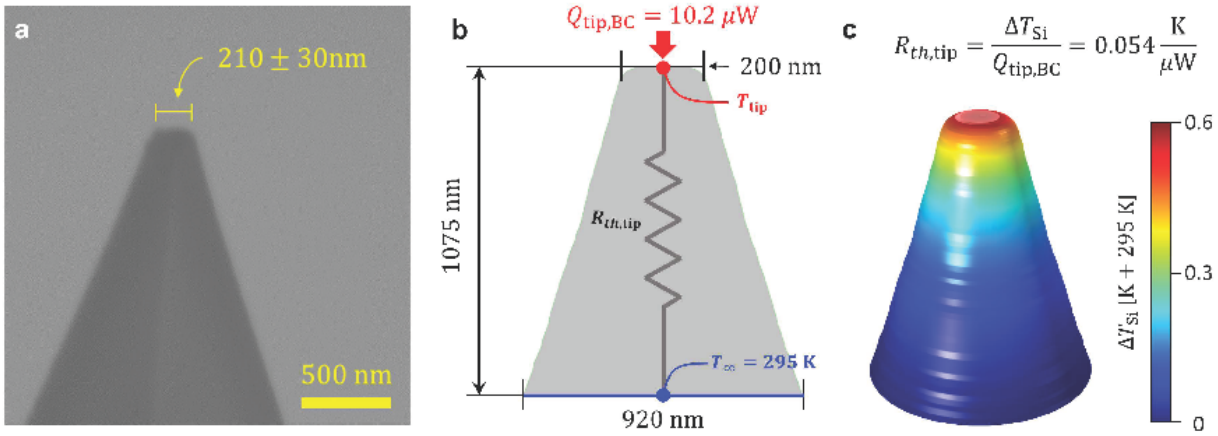

Figure 14: | **Estimation of the tip apex temperature. a,** SEM image of the Si tip used for the near-contact measurements as shown in Fig. 1b of the main text. **b,** The geometry of the Si tip in (**a**) is reproduced in COMSOL Multiphysics with the shown dimensions and boundary conditions. The tip's backside, located a distance of 1 μm away from the tip apex, is set to room temperature ($T_\infty = 295$ K), while the tip apex experiences the BC heat transfer rate of $Q_{\text{tip,BC}} = 10.2\ \mu$W. **c,** The simulated temperature distribution in the Si tip. The tip apex temperature is elevated by 0.6 K due to $Q_{\text{tip,BC}}$, which is negligible compared to the temperature gradient of the experiments (i.e., 172 K). The tip thermal resistance ($R_{th,\text{tip}}$) can be calculated as 0.054 K/μW which is more than two orders of magnitude smaller than the measured BC thermal resistance of ($R_{th,\text{BC}} \approx 17\ \text{K}/\mu\text{W}$).

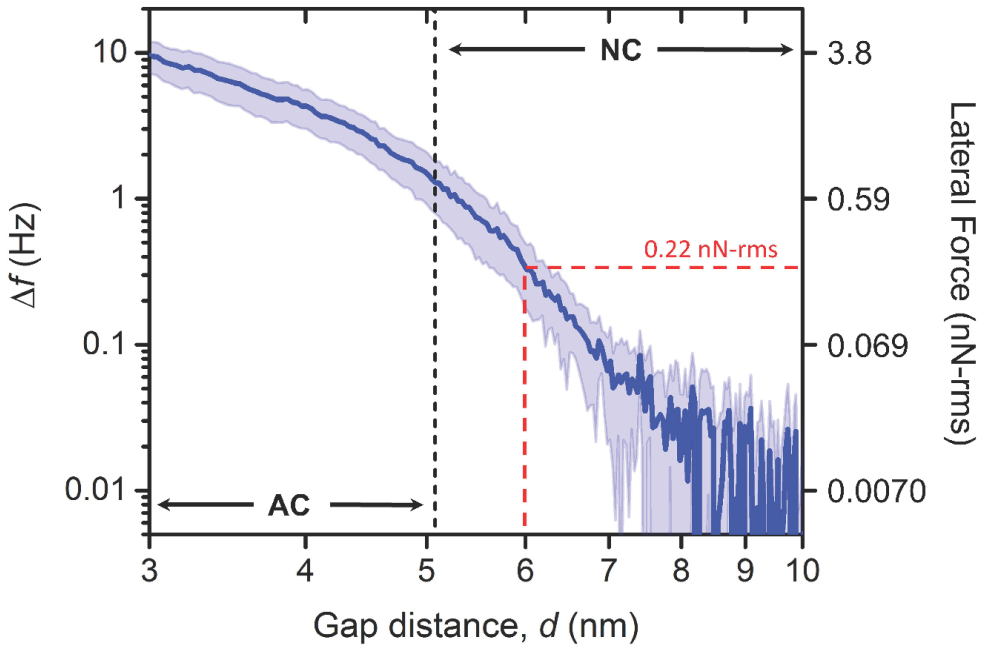

Figure 15: | **Tip-nanoheater lateral force measurement for quantitative determination of the systems surface charge density.** Log-log plot of Δf as a function of gap distance, d, between the Si tip and Pt nanoheater corresponding to the measurements presented in Fig. 2d of the Main text. The Δf signal due to tip-sample interactions can be related to the lateral force as discussed in Methods (see secondary y-axis). This demonstrates the change of lateral force with the tip-sample displacement. The near-contact (NC) gap distance of $d = 6$ nm was used to estimate the surface charge density corresponding to a tip-sample lateral force of 0.22 nN-rms.

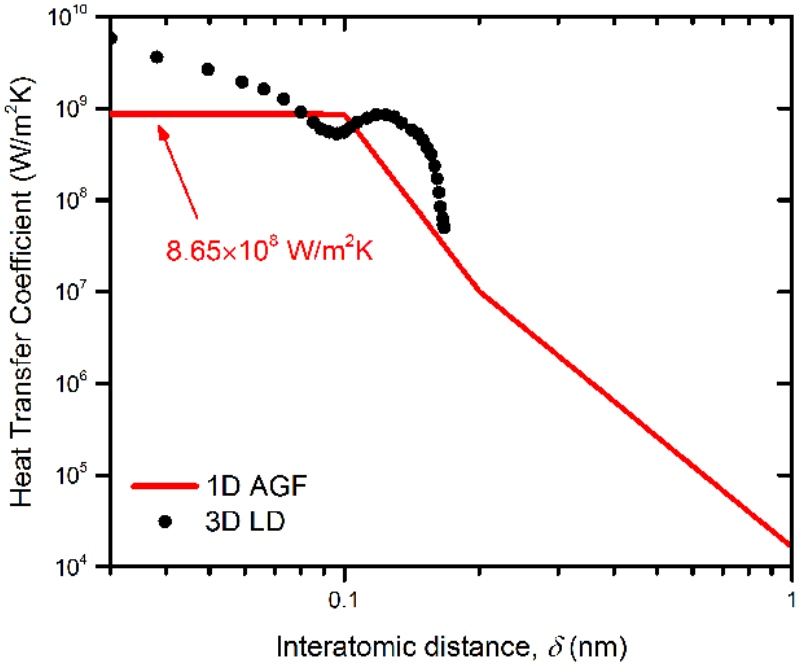

Figure 16: | **Comparison between 1D AGF and 3D LD simulations [20].** Both calculations consider two Si bulk regions separated by an interatomic vacuum distance, δ.

Table 1: | **Comparison of the Si-Si interfacial heat transfer coefficient ($h_{\text{Si-Si}}$) calculated using the 1D AGF method against results reported in the literature.**

	$h_{\text{Si-Si}}$ ($\times 10^8$ W/m^2·K)	Rel. Error (%)
3D LD ($\delta = 0.1$ nm) [20]	5.51	36.3
DMM [81]	7.28	15.8
3D AGF [80]	9.09	5.09
Exp. [82]	$1.09 \sim 7.69$	$87.4 \sim 11.1$
1D AGF [This work]	8.65	–